

Contents lists available at ScienceDirect

Geoderma

journal homepage: www.elsevier.com/locate/geoderma





Development of a lateral topographic weathering gradient in temperate forested podzols

Jennifer A. Bower^{a,*}, Donald S. Ross^a, Scott W. Bailey^b, Amanda M. Pennino^{b,c}, Michael J. Jercinovic^d, Kevin J. McGuire^{b,e}, Brian D. Strahm^b, Madeline E. Schreiber^f

- ^a Department of Plant and Soil Science, University of Vermont, 260 Jeffords Hall, Burlington, VT 05405, USA
- b Department of Forest Resources and Environmental Conservation, Virginia Tech, 210 Cheatham Hall, Blacksburg, VA 24061, USA
- ^c USDA-NRCS. 100 Centennial Mall North. Lincoln. NE 68508. USA
- ^d Department of Geosciences, University of Massachusetts, 154 Morrill Science Center, Amherst, MA 01003, USA
- e Virginia Water Resources Research Center, Virginia Tech, 210 Cheatham Hall, Blacksburg, VA 24061, USA
- f Department of Geosciences, Virginia Tech, 5048 Derring Hall, Blacksburg, VA 24061, USA

ARTICLE INFO

Handling Editor: K. Vancampenhout.

Keywords: Mineral weathering Hydropedology Podzolization Forest soils

ABSTRACT

Mineral weathering is an important soil-forming process driven by the interplay of water, organisms, solution chemistry, and mineralogy. The influence of hillslope-scale patterns of water flux on mineral weathering in soils is still not well understood, particularly in humid postglacial soils, which commonly harbor abundant weatherable primary minerals. Previous work in these settings showed the importance of lateral hydrologic patterns to hillslope-scale pedogenesis. In this study, we hypothesized that there is a corresponding relationship between hydrologically driven pedogenesis and chemical weathering in podzols in the White Mountains of New Hampshire, USA. We tested this hypothesis by quantifying the depletion of plagioclase in the fine fraction (≤2 mm) of closely spaced, similar-age podzols along a gradient in topography and depth to bedrock that controls lateral water flow. Along this gradient, laterally developed podzols formed through frequent, episodic flushing by upslope groundwater, and vertically developed podzols formed through characteristic vertical infiltration. We estimated the depletion of plagioclase-bound elements within the upper mineral horizons of podzols using mass transfer coefficients (τ) and quantified plagioclase losses directly through electron microscopy and microprobe analysis. Elemental depletion was significantly more pronounced in the upslope lateral eluvial (E horizondominant) podzols relative to lateral illuvial (B horizon-dominant) and vertical (containing both E and B horizons) podzols downslope, with median Na losses of ~74 %, ~56 %, and ~40 %, respectively. When comparing genetic E horizons, Na and Al were significantly more depleted in laterally developed podzols relative to vertically developed podzols. Microprobe analysis revealed that ~74 % of the plagioclase was weathered from the mineral pool of lateral eluvial podzols, compared to ~39 % and ~23 % for lateral illuvial podzols and vertically developed podzols, respectively. Despite this intense weathering, plagioclase remains the second most abundant mineral in soil thin sections. These findings confirm that the concept of soil development as occurring vertically does not accurately characterize soils in topographically complex regions. Our work improves the current understanding of pedogenesis by identifying distinct, short-scale gradients in mineral weathering shaped by local patterns of hydrology and topography.

1. Introduction

Weathering reactions provide life-sustaining nutrients to ecosystems, control streamwater chemistry, sequester carbon, and build soils. Young soils (<25,000 years old) formed from glacial sediments represent potential hotspots for mineral weathering because of the prevalence of

soluble minerals and exposed surfaces (Slessarev et al., 2019). Beyond age, the interplay of topography, soil structure, and hydrology is known to shape the weathering evolution of soils (van der Meij et al., 2018). The relationship between water and weathering is frequently framed in terms of variations in precipitation and evapotranspiration (Anderson et al., 2018; Chadwick et al., 2003; Norton et al., 2014), whereas few

E-mail address: jbower@uvm.edu (J.A. Bower).

^{*} Corresponding author.

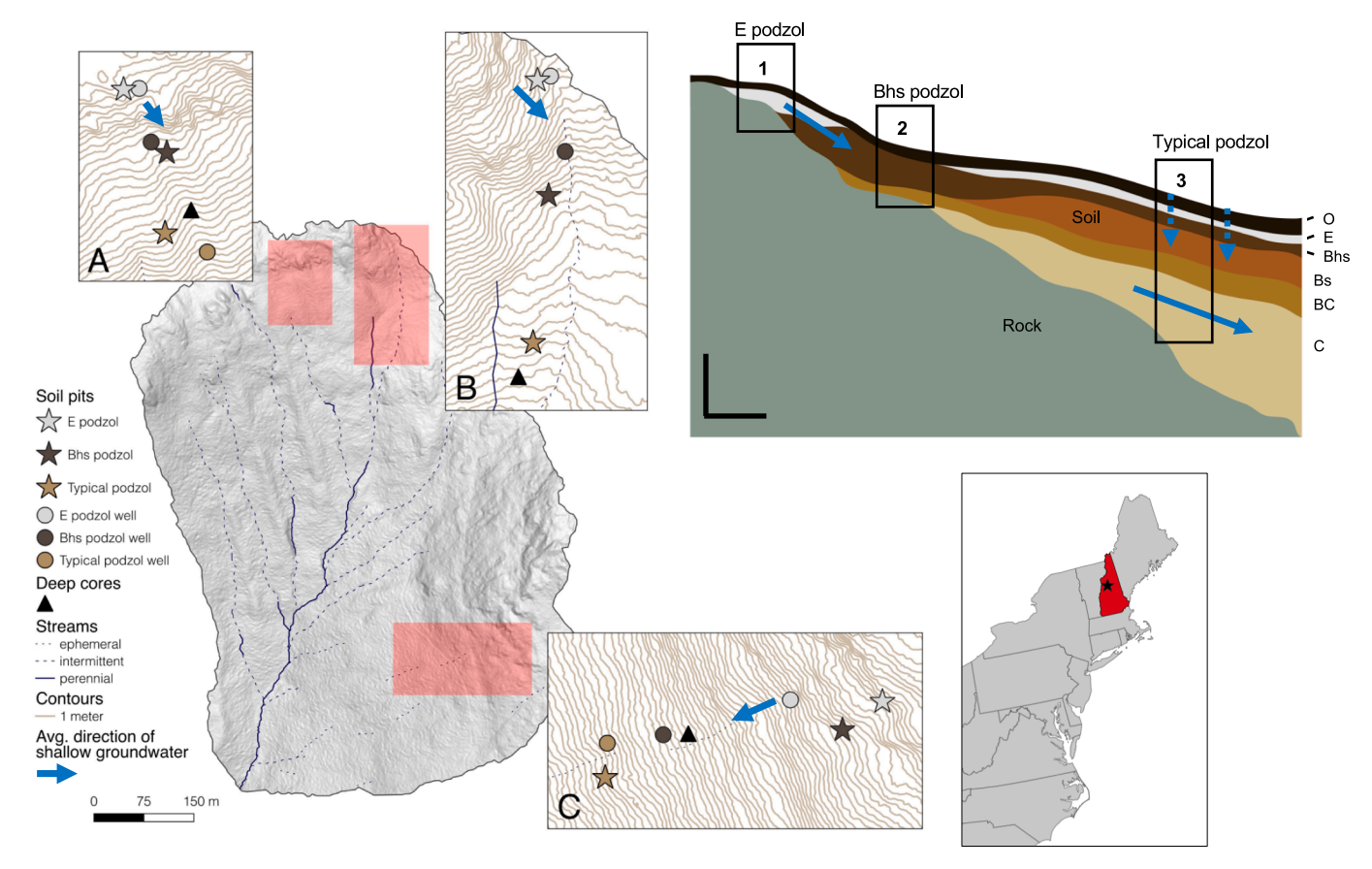


Fig. 1. At left, a map representing the locations of sampled soil pits, well pits, and deep C horizon cores in Watershed 3, Hubbard Brook, New Hampshire, USA. The map insets labeled "A", "B", and "C" represent the soil pit transects. On the map insets, stars represent podzols that were incrementally sampled and from which soil clod thin sections were collected; circles represent soil pits dug to install shallow groundwater wells that were included to improve the power of our statistical analysis as described in Section 2.3. Blue arrows represent the average direction of shallow lateral groundwater flow (Benton et al., 2022). The inset at the lower right shows the location of Hubbard Brook Experimental Forest, New Hampshire, USA. The inset at the upper right shows an example schematic of the hillslope distribution of lateral podzols (E podzols and Bhs podzols; 1 and 2) and vertical podzols (Typical podzols; 3). Soil colors (tan, brown, light gray, and black) represent soil horizons, while rock is represented in gray-green. Lateral and vertical flow is shown by arrows, after Bailey et al. (2014), Gannon et al., (2014), and Gannon et al. (2017). In this study, lateral E podzols consist of thick E horizons with no B horizons; lateral Bhs podzols consist of a thick Bhs, with or without a thin E above it; Typical podzols consist of a thin (≤10 cm) E, thin Bhs, followed by a Bs. The vertical and horizontal scale bars represent 0.5 m and 10 m, respectively.

field studies examine the influence of local gradients in water and associated solute flux on primary mineral weathering in soils. This may be particularly important in mountainous, forested systems, where soil expression and saturation conditions change rapidly over short distances (Gannon et al., 2014; Villars et al., 2015). Weathering rates depend on water flux and water residence, with shorter water residence times producing higher weathering rates (Maher, 2010). In turn, topography and catchment geometry affect water flux and water residence (McGuire et al., 2005; Remondi et al., 2019). For these reasons, it is necessary to look beyond precipitation and evapotranspiration to understand weathering in soils at the hillslope scale.

Weathering studies frequently consider soil as forming from rock and regolith through top-down processes (e.g., Brantley and White, 2009; Yoo and Mudd, 2008). In soil-mantled landscapes at steady state, where groundwater is limited to a deep saturated zone, many biogeochemical models assume infiltration is essentially vertical (Wallman et al., 2005). These assumptions fail where subsurface lateral water flow is important, such as in coarse-textured soils over shallow bedrock, where the land surface is steeply sloping, where a restrictive soil horizon limits vertical infiltration, or in low-lying areas (Benton et al., 2022; Do Nascimento et al., 2008; Freer et al., 2002; Weyman, 1973). In such environments, weathering products are transported laterally and the degree of pedogenesis is reflective of local patterns of subsurface flow (Bailey et al., 2014; Bourgault et al., 2017; Lin et al., 2006; Park and Burt, 2002). In tropical podzols, lateral pedogenesis was discovered to be linked to

lateral weathering across gradients in drainage and topography, demonstrating a relationship between local hydrologic patterns and weathering (Chauvel et al., 1987; Fritsch et al., 2011). Although the effects of lateral subsurface flow have been considered within hydrologic and hillslope evolution models (e.g., Harman and Cosans, 2019; Salve et al., 2012), such models often assume soil properties are constant across the hillslope and tend to focus on weathering reactions along deep flowpaths rather than in the shallow solum.

Bailey et al. (2014), working in the White Mountains of New Hampshire, USA, found that soil morphology was linked to the dominance of lateral flow within shallow podzols in a steep catchment. They observed that the water table rose into the solum (E and B horizons) of shallow podzols dominated by either a thick E or a thick B horizon during rain events. In contrast, the water table never entered the solum in deeper, well-drained podzols, implying a link between saturation dynamics and pedogenesis. A number of studies have observed lateral podzolization in topographically complex areas in Europe and the USA, suggesting that this process is a widely distributed phenomenon among temperate podzols (Bourgault et al., 2015; Jankowski, 2014; Sommer et al., 2001; Sommer et al., 2000). In studies examining temperate lateral podzolization, lateral eluvial (E horizon dominant) podzols are common at the top of the hillslope, lateral illuvial podzols (Bhs horizon dominant) are located immediately downslope from eluvial podzols, and vertical podzols occur in downslope areas that are not significantly influenced by lateral water fluxes in the solum (positions 1, 2, and 3 in

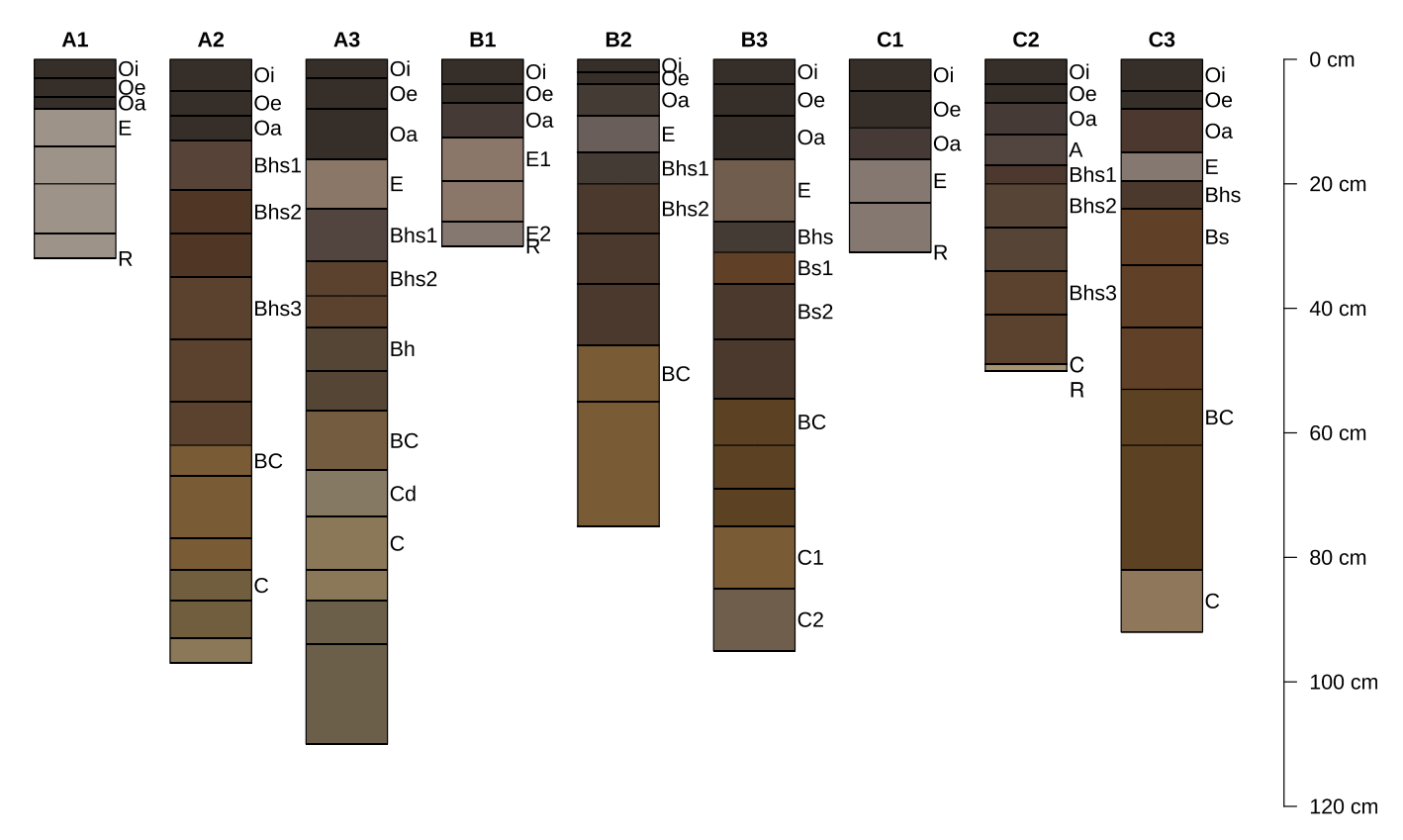


Fig. 2. Pedons sampled within the study. Within soil pit labels, letters represent transects, and 1 represents E podzols, 2 represents Bhs podzols, 3 represents Typical podzols. Horizons were sampled at every increment displayed. For simplicity, genetic horizons are aggregated and labeled according to the horizon described in the field. R represents bedrock. Only samples obtained above 100 cm are shown for legibility.

the catena image in Fig. 1). Laterally formed podzols experience frequent, episodic saturation by shallow, acidic groundwater, whereas vertical podzols rarely saturate fully (Bailey et al., 2014; Gannon et al., 2017). Given the influence of water on relative weathering intensity, we hypothesized that a mineral weathering gradient occurs across the hillslope.

The goal of this work was to compare primary mineral weathering in podzols across this hypothesized lateral weathering gradient, with a focus on plagioclase because of its abundance and solubility. We predicted that plagioclase weathering would be most pronounced in laterally developed soils that experience high saturation frequency and least pronounced in vertically developed soils where groundwater rarely rises above the C horizon. To test this, we measured plagioclase weathering in the fine fraction of soils (≤2 mm). Our work builds on prior studies in the same study area that investigated hillslope differences in soil morphology, chemistry, and hydrologic behavior (e.g., Bailey et al., 2014; Bourgault et al., 2015; Gannon et al., 2014).

2. Materials and methods

2.1. Site description

Soils were examined at three field sites in Watershed 3, in the northeastern part of the Hubbard Brook Experimental Forest (HBEF), a long-term ecological research site in central New Hampshire, USA, with a stream chemistry record spanning six decades (Fig. 1). Watershed 3 is a gauged watershed that serves as the hydrologic reference catchment for the long-term HBEF study. The annual average precipitation at HBEF is 1400 mm, and the climate is currently classified as humid continental with mean daily temperatures of $-8.3\ ^{\circ}\text{C}$ in winter and $18.7\ ^{\circ}\text{C}$ in summer (A.S. Bailey et al., 2003). Tree cover in shallow-soil areas is mainly mixed coniferous, consisting of Abies balsamea (L.) Mill. (balsam

fir), *Picea rubens* Sarg. (red spruce) and *Betula cordifolia* Regel (mountain white birch), and transitions in deeper soils to a Northern mixed hardwood forest containing *Fagus grandifolia* (American beech), *Betula alleghaniensis* Britt. (yellow birch), and *Acer saccharum* Marsh. (sugar maple).

The soil parent material consists of same-aged sandy loam glacial till deposited during glacial retreat at the end of the Wisconsinan phase of Pleistocene glaciation, ca. 14,000 years ago. The till was deposited on top of bedrock consisting of sillimanite-grade pelitic schist and calcsilicate granulite of the Silurian Rangeley Formation (Burton et al., 2000). The main contributing lithology to the parent material is Devonian-age Kinsman granodiorite, followed by schists of the Rangeley Formation, Ordovician-age Ammonoosuc volcanics, and minor amounts of local diabase dikes and pegmatite (S.W. Bailey et al., 2003). Though glacial drift is relatively uniform in composition across the HBEF experimental watersheds, it varies in thickness across the landscape, resulting in soil depths of 0-3 m. Upslope soils are dominated by organic mats over bedrock and soils with eluvial (E) horizons that are either lacking a B horizon or have E horizons proportionally thicker than the cumulative underlying B horizons (corresponding to lithic Histosols and E podzols named by Bailey et al. (2014), respectively). These soils are accompanied by frequent saturation with acidic water enriched in dissolved organic carbon (DOC) and cations including aluminum (Al) and iron (Fe), the latter which are hypothesized to be products of bedrock weathering (Bailey et al., 2019a). Immediately downslope, Bhs podzols contain illuvial B horizons that are proportionally thicker than the overlying E horizons, when present, with the lowest B horizon underlain by bedrock or C horizon of variable thickness. Further downslope, the most common soils are characteristic of podzols generally (Typical podzols), with an E horizon overlying a sequence of B horizons (often Bhs-Bs-BC) that are thicker than the E horizon. Here, the thickness of glacial drift overlying bedrock varies up to ten meters and the water

Table 1
Abbreviated pedon descriptions and chemical data for solum mineral horizons of the podzols sampled within this study. The chemical properties of fourteen C horizon samples are averaged at the bottom of the table and represent the reference used for calculating depletion. C horizon was collected from the base of two Bhs podzol pits, three Typical podzol pits, and three deep boreholes. Bedrock was encountered at the base of all three E podzol pits, and one Bhs podzol pit. Asterisks represent horizons that were sampled incrementally. Where horizons were sampled incrementally, chemical analyses were depth-averaged.

Pedon	Soil unit	Horizon	Top (cm)	Base (cm)	Ca (mg/kg)	Na (mg/kg)	Al (mg/kg)	Ti/(Ti + Zr)	τСа	τNa	τAl
A1	E podzol	E*	8	32	4100	8900	44,300	0.92	-0.77	-0.73	-0.63
A2	Bhs podzol	Bhs1	13	21	4900	10,000	46,600	0.93	-0.63	-0.60	-0.47
		Bhs2*	21	35	5400	10,200	53,600	0.94	-0.57	-0.57	-0.36
		Bhs3*	35	62	7600	13,300	57,700	0.93	-0.24	-0.31	-0.14
A3	Typical podzol	E	16	24	4600	11,700	48,900	0.93	-0.62	-0.50	-0.40
		Bhs1	24	33	5100	11,700	50,000	0.95	-0.64	-0.57	-0.47
		Bhs2*	33	43	5800	11,100	48,600	0.94	-0.45	-0.38	-0.26
		Bh*	43	57	7300	8200	43,300	0.93	-0.15	-0.14	+0.04
B1	E podzol	E1*	13	26	2500	12,300	51,400	0.93	-0.86	-0.78	-0.63
		E2	26	30	2500	14,200	59,900	0.93	-0.85	-0.77	-0.64
B2	Bhs podzol	E	9	15	4600	7900	45,300	0.91	-0.68	-0.59	-0.49
		Bhs1	15	20	4600	7400	41,400	0.95	-0.71	-0.73	-0.59
		Bhs2*	20	46	6600	11,500	53,800	0.93	-0.49	-0.53	-0.38
В3	Typical podzol	E	16	26	4300	11,400	44,900	0.92	-0.60	-0.45	-0.37
		Bhs	26	31	5200	12,000	48,000	0.95	-0.52	-0.42	-0.34
		Bs1	31	36	5900	12,100	51,000	0.92	-0.43	-0.38	-0.25
		Bs2*	36	55	6100	12,300	54,500	0.93	-0.28	-0.24	-0.05
C1	E podzol	E*	16	31	7100	10,300	49,300	0.96	-0.68	-0.75	-0.66
C2	Bhs podzol	Bhs1	17	20	5800	11,800	55,500	0.94	-0.63	-0.60	-0.46
02	Diis pouzoi	Bhs2*	20	34	6200	12,300	52,800	0.93	-0.51	-0.49	-0.38
		Bhs3*	34	49	6600	13,300	51,200	0.93	-0.34	-0.30	-0.23
C3	Typical podzol	E	15	20	4800	11,600	45,400	0.92	-0.62	-0.51	-0.25
55	1 y pictii pouzoi	Bhs	20	24	6500	12,500	49,800	0.93	-0.52	-0.53	-0.47
		Bs*	24	53	7400	14,000	58,200	0.93	-0.36	-0.36	-0.24
Reference average	_	C	-	-	9300	17,700	62,200	0.93	-	-	-

table rarely rises above the C horizon. The lateral distance from the lithic Histosols and E podzols to the nearest Typical podzols typically ranges from 40 to 200 m.

The distribution of these soils is strongly predicted by lidar-derived topographic metrics, enabling spatial patterns to be modeled with high accuracy (Gillin et al., 2015a). The topographic metrics that are most effective at modeling soil distribution include topographic position, topographic wetness, Euclidean distance to bedrock, and upslope accumulated area. The effectiveness of these specific metrics in predicting soil type within the study area reflects the tight relationship between topography, water table behavior, and soil patterning (Bailey et al., 2019a; Gillin et al., 2015b). Areas of bedrock outcrops and associated shallow soils in this area have been successfully modeled using similar metrics (Fraser et al., 2020). These predictive models informed our preliminary fieldwork and sampling design.

2.2. Field sampling

Nine soil pits were dug within Watershed 3 (Fig. 1). With reference to the soil model developed by Gillin et al. (2015a), soil pit sites were selected to include 3 E podzols, 3 Bhs podzols, and 3 Typical podzols (starred locations on the map in Fig. 1). The R package aqp was used to display profiles for reference in Fig. 2 (Beaudette et al., 2013). One soil selected as a Typical podzol keyed out as a different type of podzol based on the presence of a Bh horizon below the Bhs horizon (Bimodal podzol; refer to Bailey et al., 2014), but according to nearby well data, it matched the well-drained characteristics of Typical podzols. All soil pits were described in the field by genetic horizon according to Schoene-berger et al. (2012). The full profile descriptions are given in Bower et al. (2023a).

Descriptive characterization of soil pedons included moist Munsell color (determined under sunlight when possible), texture, structure, moist consistence, presence of redoximorphic features, rooting density, depth to root restriction, and coarse fragment content. Soils were characterized using a color-based approach following Bailey et al.

(2014). When describing genetic B horizons, an 's' subhorizon designation was assigned for a hue 7.5YR or redder; 'h' if value and chroma were both 3 or less; and 'hs' if both conditions applied. An 'h' alone horizon designation was described using the original classification for a soil color 3 or less in value and chroma and 10YR in hue. Munsell color and texture were also used to describe variation within deep subsoil samples. When laboratory data were received after sampling for laboratory analysis using the methods described below, Oa horizon designations were revised to A horizons if they contained less than 200 g kg⁻¹ organic carbon by weight, and vice versa in accordance with NRCS taxonomic criteria (Bower et al., 2023a; Soil Survey Staff, 2022).

To detect variations in elemental concentration by depth within genetic horizons, soil samples were collected using the following approach. If a solum horizon (excluding BC and C horizons) was greater than 10 cm in thickness, it was subsampled by dividing it into increments of 6–10 cm to detect potential intra-horizon chemical variation (VandenBygaart et al., 2007). Intact, oriented soil clods were gently gathered in duplicate from pit locations by genetic horizon. Due to complications processing soil clods, four pits were re-sampled for soil clods by re-digging pits less than a meter away and confirming the soil horizons in new pits agreed with the previous pit descriptions. C horizons were sampled with a 51 mm diameter bucket auger or 51 mm diameter Shaw drill by depth interval at pit bases if bedrock was absent. In addition, deep cores were collected from 51 mm split-spoon samples incrementally obtained by depth during well installation using a trackmounted drill rig with 102 mm hollow-stem augers. These deep cores were located near pits (locations marked with black triangle symbols in Fig. 1). The location of all sampling points was determined using a Trimble GPS unit with an external hurricane antenna and postprocessing for 1 m precision.

2.3. Soil chemical analyses

The following chemical analyses were conducted upon dried soil samples sieved through 2 mm mesh, except where noted. pH was

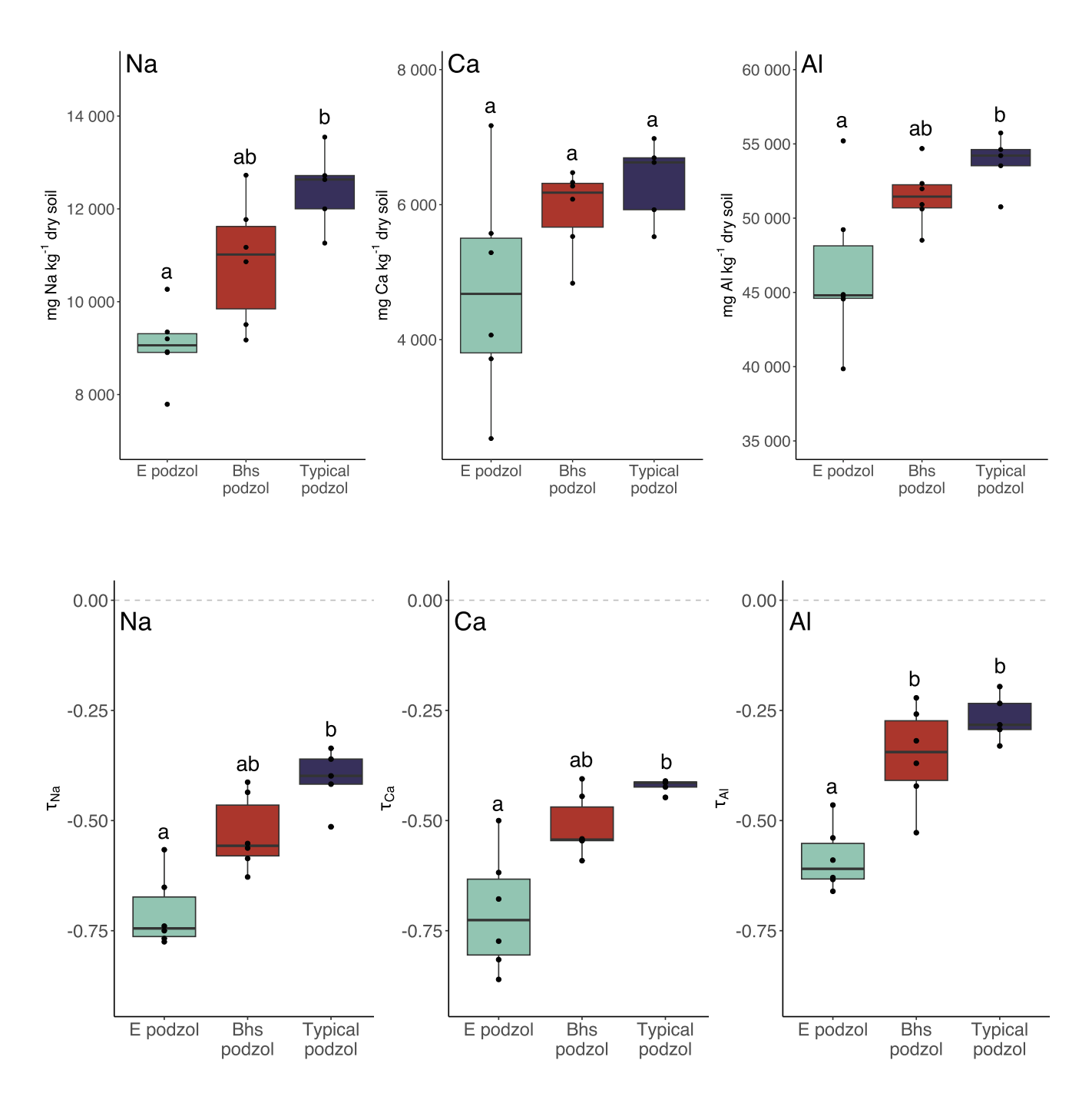


Fig. 3. Upper: total Na, Ca, and Al from elemental digestion of samples from 17 podzols compared by podzol type (E podzol n = 6; Bhs podzol n = 6; Typical podzol n = 5). Note the difference in y-axis scales between plots. The horizontal lines represent the median, colored boxes show the interquartile range, vertical lines give the minimum and maximum, and dots are outliers. For the purposes of comparing profiles, E, Bh, Bhs, and Bs horizons were included in analysis. The letters a and b denote significant differences among medians at p < 0.05. Lower: Boxplots comparing elemental depletion among podzols. Letters indicate significance, with a and b differing significantly at p < 0.05. Again, O, A, Bw (only in one pit), BC, and C horizons were excluded from analysis (with E, Bh, Bhs, and Bs horizons remaining).

determined with a glass electrode in a 2:1 solution of 0.01 *M* calcium chloride to dry soil (Richter et al., 1988). Soils were combusted for total carbon using an Elementar Vario Max CNS Elemental Analyzer at Virginia Tech to confirm field determination of mineral horizon identity and estimate bulk density. Bulk density was calculated from carbon concentrations using the strong relationship identified for HBEF soils, supported by later analysis (Federer et al., 1993; Brousseau, unpublished data). To obtain total concentrations of major and trace elements, 20 mL

of soil samples were sent to Activation Laboratories in Ancaster, Canada. There, samples were fluxed with lithium metaborate/tetraborate, diluted in a weak nitric acid solution, and analyzed by ICP-OES and ICP-MS for major and trace elements. To enhance the statistical power of between-horizon elemental depletion comparisons, soil samples from 8 additional pits representing the podzol types of interest (circle locations in Fig. 1) described and sampled by the same team that worked the original 9 pits were digested by Activation Laboratories using the same

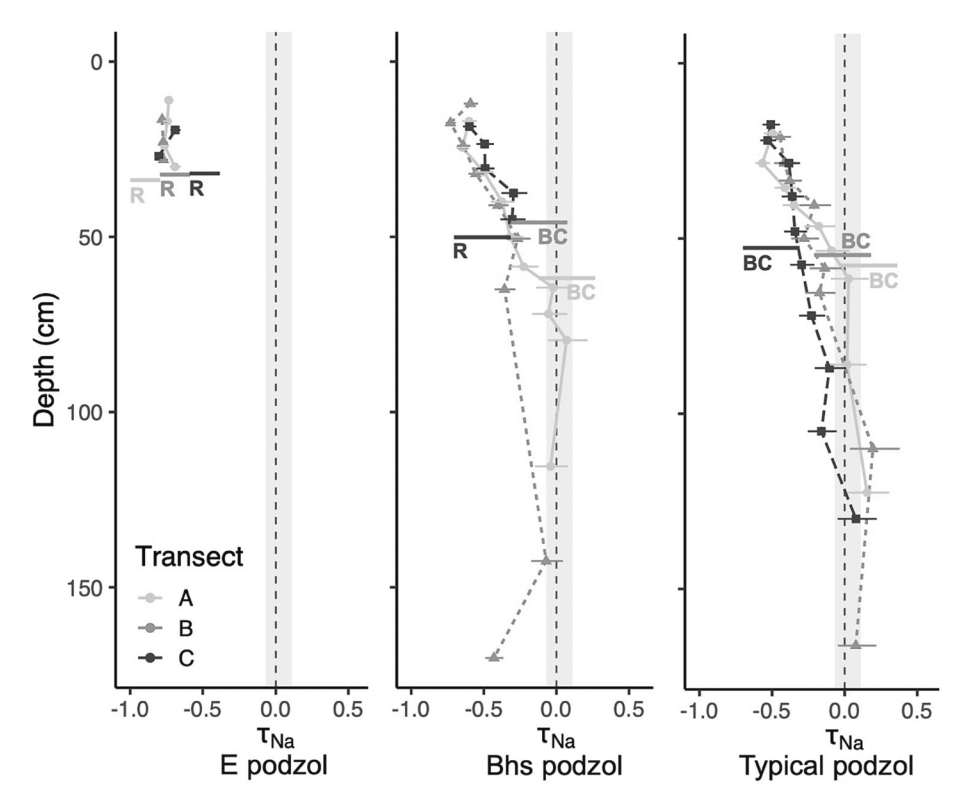


Fig. 4. Change in Na (τ_{Na}) plotted against depth for the 9 pits that were subsampled by horizon. The dotted line represents 0 net depletion of Na, with -1 representing total depletion and 1 representing a doubling of Na. The 95% confidence interval for the reference samples used to calculate depletion is in light gray and error bars estimated from deep reference samples are shown as horizontal bars around points. The bottom of the solum as defined in this manuscript is given by lines labeled by R (indicating the bedrock interface) and BC (indicating the top of the transitional horizon above C horizon).

method. These soil pits were excavated during the process of installing shallow wells near the original soil pits and were selected to represent the same soil types. They would have totaled 9 like the original pits, but one soil did not meet the morphology criteria because it was in the middle of an ephemeral stream and so was removed from our analysis.

Before testing for chemical differences, data were assessed for normality using the Shapiro-Wilk test, and nonparametric tests were chosen for statistical analysis. We compared the significance of differences between soil profiles and genetic horizons using the Kruskal-Wallis analysis of variance and Dunn's *post-hoc* test for pairwise comparisons, corrected by the Holm-Bonferroni method. When multiple incremental samples were taken from the same genetic horizon, they were depth-weighted and averaged. This was performed by multiplying each value by the incrementally sampled horizon thickness, summing, and dividing by the total genetic horizon thickness. In the case of whole profiles, every horizon was depth-weighted down to the top of the BC or C horizon (base of solum). Only E, Bh, Bhs, and Bs horizons were summed (Fig. 2). All calculations were done in R using the reshape package and packages from the tidyverse set of packages (R Core Team, 2022; Wickham, 2007; Wickham et al., 2019).

2.4. Quantification of elemental depletion

Bulk elemental concentrations in soil samples were used in conjunction with deep (>1 m) C samples to estimate fractional loss based on the mass loss approach developed by Brimhall and others (Brimhall et al., 1991; Brimhall and Dietrich, 1987). This method was applied to all 17 pits for which elemental data was available. Losses or additions of the element of interest are represented by tau (τ_j), calculated from the proportion of the concentration of the element of interest (j) to the concentration of the index element (i) in weathered (w) materials (representing solum horizons) and parent (p) materials (representing C horizons; Eq. (1)).

$$\tau_j = \frac{\left(j_w \times i_p\right)}{\left(j_p \times i_w\right)} - 1 \tag{1}$$

Depletion of the element of interest is indicated by values less than 0, with enrichment indicated by values greater than 0.

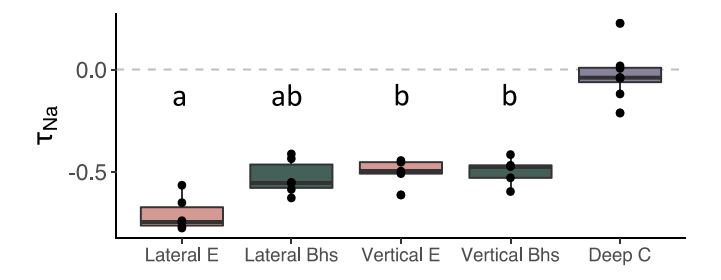
This method assumes negligible loss or additions of the selected index element and homogenous composition of the parent material. After evaluating Ti, Zr, and Nd as potential index elements, Ti was chosen for τ calculations because it was highest in concentration and thus less influenced by analytical error. Although mineral phases containing index elements are resistant to dissolution, the assumption of immobility does not always hold, such as when index-element-bearing minerals are fractionated into particle sizes that are more susceptible to transport (Taboada et al., 2006). Microscopic analysis provided some insight into the size fractionation of Ti-bearing minerals within this study, which is discussed further in Appendix A. Variation of index elements with depth was compared by calculating the normalized ratio, represented below by R, of Ti and Zr concentrations:

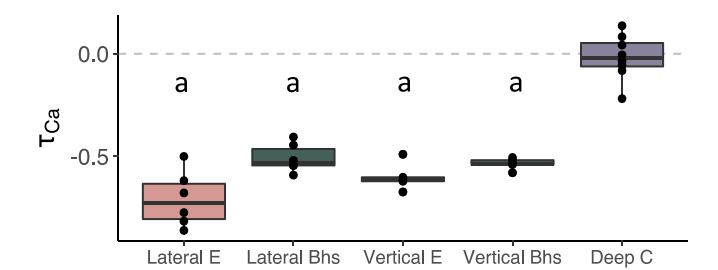
$$R_{Ti/(Ti+Zr)} = \frac{[Ti]}{[Ti] + [Zr]}$$
 (2)

This ratio indicates preferential mobilization of one element over the other (Bern et al., 2011). There appeared to be slight mobility of Ti and Zr with respect to each other within certain profiles, an observation that is discussed in full detail in Appendix A. The scripts used to calculate tau are available online (Bower, 2023).

2.5. Microscale approach

To examine mineral weathering directly at the mineral grain scale, intact (unsieved) soil clods around 4–6 cm at their widest diameter were prepared and analyzed using the following techniques. After collection,





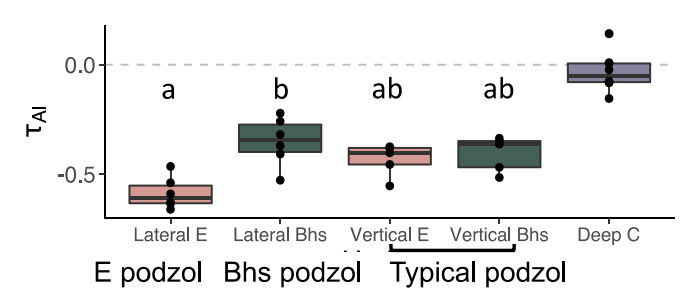


Fig. 5. Boxplots of τ (depletion) for selected plagioclase-bound elements, compared by genetic soil horizon and by lateral and vertical development. Letters indicate significant differences among medians, with a and b differing significantly at p < 0.05. Although C horizons are shown, they were not included within the comparison because τ is based on their average, thus they have no letter denoting significance.

intact soil clods were dried at 70 °C, impregnated with Scotchcast TM #3 electrical resin in a desiccator under vacuum, and cured overnight in an oven at 105 °C. A total of 65 soil and subsoil clods and 3 additional subsoil cores were shipped to Spectrum Petrographics for thin section preparation. Thin sections were ground to 30 μm and polished for x-ray analysis. Thin sections were digitally scanned in high resolution using a macroscope and investigated using petrographic and micromorphological approaches described by Stoops (2021) and Delvigne (1998).

Alteration of plagioclase grains was described for selected thin sections in transect A (8 slides total) using a JEOL 6060 Scanning Electron Microscope (SEM) with Oxford Energy Dispersive Spectroscopy (EDS) attachment at the University of Vermont Microscopy Imaging Center. Within each slide, 15-20 plagioclase grains were chosen from 4 to 6 areas because of their proximity to minerals investigated with SEM to validate electron microprobe analysis (EPMA) maps, as described later. The degree of alteration was classified on a scale of 0-4 by modifying the approach by Stoops et al. (1979) for describing mineral alterations. Given the young age of these soils, the scale presented by Stoops et al. (1979) for describing alteration was subdivided into 0.5-point subdivisions to allow for a finer resolution of description. Class 0 represents an unaltered or nearly unaltered mineral; class 1 represents a slightly altered mineral; class 2 represents a moderately altered mineral; class 3 represents a strongly altered mineral; and class 4, which is unobservable in the case of dissolution, would represent a completely altered (dissolved) mineral. No classes beyond 2.5 were observed. Examples of plagioclase grains and their corresponding alteration grades are given in

Fig. A1.

EPMA with Wavelength Dispersive Spectroscopy (WDS) was performed by a Cameca SX-five-Tactis with five wavelength dispersive spectrometers at the University of Massachusetts at Amherst. Twenty-six soil thin sections were scanned in full (\sim 20 mm \times 17 mm) using a 30 μ m by 30 µm pixel resolution. Thin sections were selected to include one from each genetic horizon of the solum for all pits and five total subsoil samples, three of which came from >2 m drilled boreholes. The elements measured by WDS were Si, Al, Fe, Na, and Ca. In tandem with WDS, energy dispersive spectrometry (EDS) was used to collect a spectrum at each pixel, from which semi-quantitative estimates of additional elements were gathered using a peak fitting approach. These additional "hypermap" elements included K, Mg, Mn, P, Ce, and Ti, and were collected across all slides except for two, which were scanned before the hypermap approach was employed. The procedure for quantifying the WDS elements is described in Appendix A. Hypermap elements estimated from EDS spectra were not quantified but instead retained as raw counts to enable coarse detection of relative abundances. The goal of this approach was not to achieve a high accuracy quantitative analysis of every mineral present, but rather to evaluate mineral abundances and compare compositional and mineralogical trends.

EPMA data were used to estimate mineral abundance for each slide by modifying the method described by Bailey et al. (2019b). Minerals were identified by importing cluster information into R (R Core Team, 2022), estimating the elemental content of each cluster using the standard curves described above using packages from the tidyverse set of packages (Wickham et al., 2019), and using a series of scripted rules to identify mineral species based on the presence, abundance, and proportion of certain elements. Additional details regarding this process are given in Appendix A. SEM-EDS was used to groundtruth mineral assignments and identify unknown minerals to refine rule-based cluster identification using an iterative approach described in Appendix A. During this exercise, we identified secondary oxides as well as phases with stoichiometry suggestive of organometallic complexes. No clay minerals were found using this process, in line with other findings of low (<5%) clay content in podzols of the Northeast (April et al., 1986), although minor amounts of clays were likely present.

Mineral abundance and stoichiometry were used to calculate elemental abundance using a series of calculations following the approach by Bailey et al. (2019b). The percentages of each of the five main (non-EDS) elements were converted to percent oxides and summed to estimate the total oxide composition within each cluster. Phases were aggregated according to cluster identity and summed by pixel number, with mineral content and void also summed. Area mineral abundance was converted to mass percent by accounting for the specific gravity of individual minerals using Deer et al. (2013). Because storage of Na in secondary phases and exchange sites is low, and it is commonly used as a proxy for plagioclase, it was selected for additional calculations. The percentage of Na in each phase was multiplied by the mineral area of each phase to estimate the Na content of the mineral-only fraction. This was then divided by the sum of Na for all phases to estimate the percent contribution of each phase to the total. The Na contribution from each phase in mg kg⁻¹ was estimated by multiplying the Na contribution from each mineral by its abundance in mass percent. This was summed and total Na of each slide was compared to total Na obtained from elemental digestion.

The proportion of Na contributed by plagioclase in thin sections was used in conjunction with total elemental data to estimate fractional mass loss of plagioclase within each pit. Quartz and plagioclase mass percentages were separately used to estimate fractional mass loss of plagioclase for comparison. A greater volume of sample was collected at a higher resolution for total elemental analysis than epoxied soil clods, and therefore per-mineral Na mass percentages attained by EPMA were used to partition digestion-derived total Na into mineral pools. EPMA results were applied to similar genetic horizons within pits (e.g., the same proportion used for all Bs horizons in a pit given coarse sampling

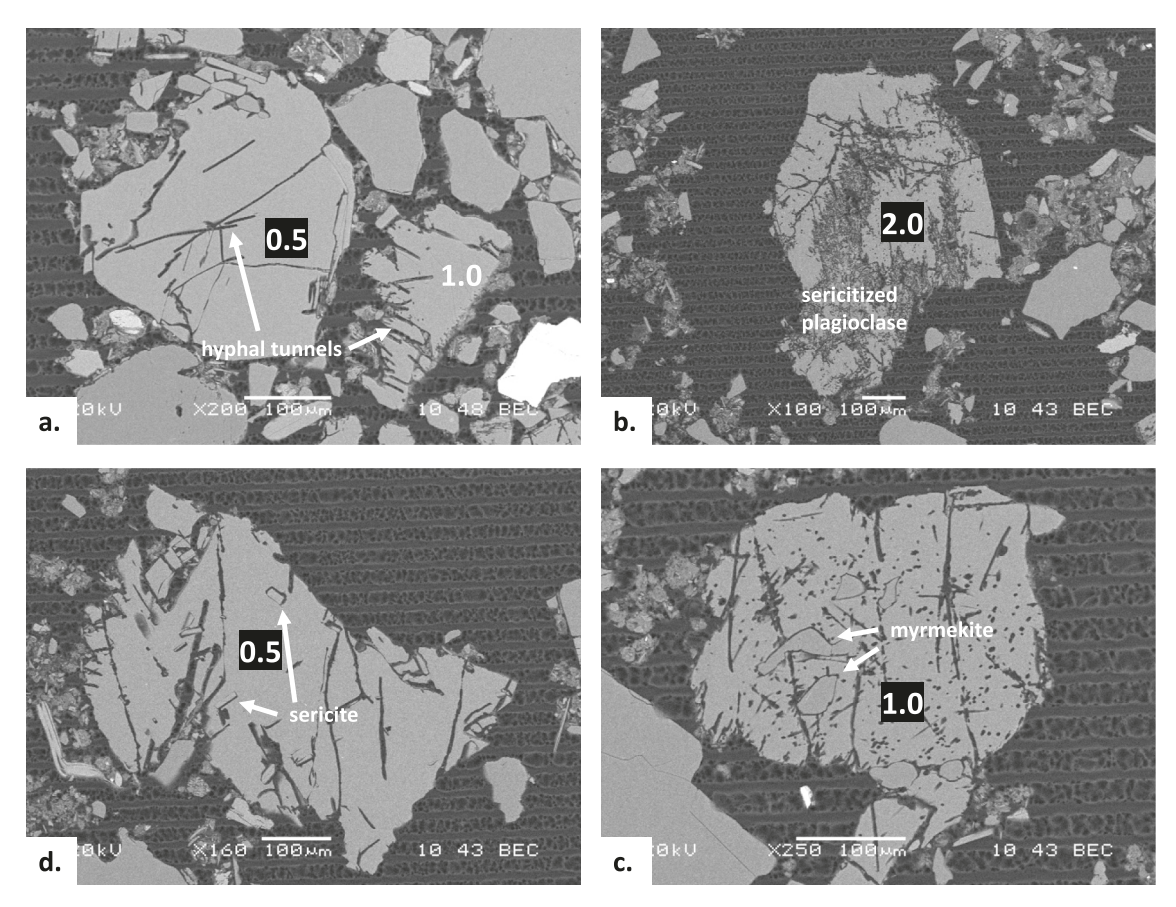


Fig. 6. Weathering features in plagioclase grains shown through SEM microphotographs. Alteration scale ratings are given in the white numbers highlighted in black. Clockwise from top left: a. two plagioclase grains showing evidence of mycorrhizal tunneling; b. heavily pitted plagioclase grain; c. plagioclase grain showing microporosity around myrmekite (small worm-shaped quartz intergrowths); d. plagioclase grain showing microporosity around tabular sericite grains. The top left image is from a BC horizon at the base of a Bhs podzol and the other three images are from horizons of a Typical podzol.

density) and averaged for transitional horizons. After partitioning total elemental data by phase, a stoichiometric scaling factor determined from SEM-EDS results (0.81 mol Na per 1 mol plagioclase) was employed to estimate mineral abundance in mg kg $^{-1}$. This enabled analysis of plagioclase depletion based on the index element method described above. It should be noted that this approach assumes there is negligible Ti in plagioclase, which was confirmed here through point analysis with SEM-EDS and WDS. Independently, quartz was used as an index to estimate plagioclase losses in soil clods. These were compared with Ti-based values, and not scaled to whole pits.

3. Results

3.1. Elemental trends

Soil elemental composition showed expected weathering-induced differences between solum horizons (i.e., excluding BC and C horizons) and parent material (C horizons), as well as differences between podzol types. Na, Ca and Al were lowest in E podzols, except for one pit that was high in both Ca and Ti (Table 1). Concentrations in the solum for all three elements increased downslope within each transect (Fig. 3). A nonparametric Kruskal-Wallis test revealed this increase to be significant when comparing the median Na and Al content of E podzols against the medians of Typical podzols (p=0.004 and p=0.044, respectively). Complete data are given in Bower et al. (2023b).

Depletion trends of Na, Ca, and Al differed when comparing different soil types along the transects, but closely matched depth trends of τ for other pits in the same soil type. Horizon τ values are presented in Table 1, with complete data given in Table A1 Depth trends for τ_{Na}

among soil types are shown in Fig. 4. Calculated E podzol τ values for all three elements were negative, around -0.6 to -0.9 (Table 1; Table A1), and uniform with depth until bedrock (29–32 cm). This contrasted with τ values of Bhs and Typical podzols, which were negative near the soil surface and gradually approached the dotted line, representing zero depletion, towards the base of the solum (defined as the top of the BC or C horizon, 46–62 cm; marked with lines on Fig. 4). In the case of Na, Bhs podzols were more depleted than Typical podzols near the soil surface, with τ values reaching -0.6 for Bhs podzols vs. -0.5 for Typical podzols. One Bhs podzol that contained bedrock at the pit base (50 cm) exhibited a similar depth trend and similar τ values as deeper Bhs podzols until the soil-bedrock interface, without attaining a net zero-depletion value of 0 as in the case of the others.

By comparing τ of genetic horizons, we found significant differences in depletion among the medians of laterally and vertically developed horizons. Laterally eluviated horizons were found to be significantly more depleted in Na (median = -0.74) than vertically eluviated horizons (median = -0.50; p=0.040; Fig. 5). Lateral E horizons were also found to be more depleted in Na than vertical B horizons (p=0.035). In the case of τ_{Al} and τ_{Ca} , lateral eluvial horizons trended slightly more depleted than vertical eluvial horizons, differences that were not statistically significant (p=0.258 and 0.720, respectively). Median depletion in lateral eluvial horizons trended lower than median depletion of lateral illuvial and vertical illuvial horizons for all three elements, a difference that was significant for Na in vertical illuvial horizons and Al in lateral illuvial horizons (Fig. 5).

When we depth-weighted τ for the entire solum and compared soils (Fig. 3), we found significant differences in depletion. The largest losses of Na and Ca were observed in E podzols, with median depth-integrated

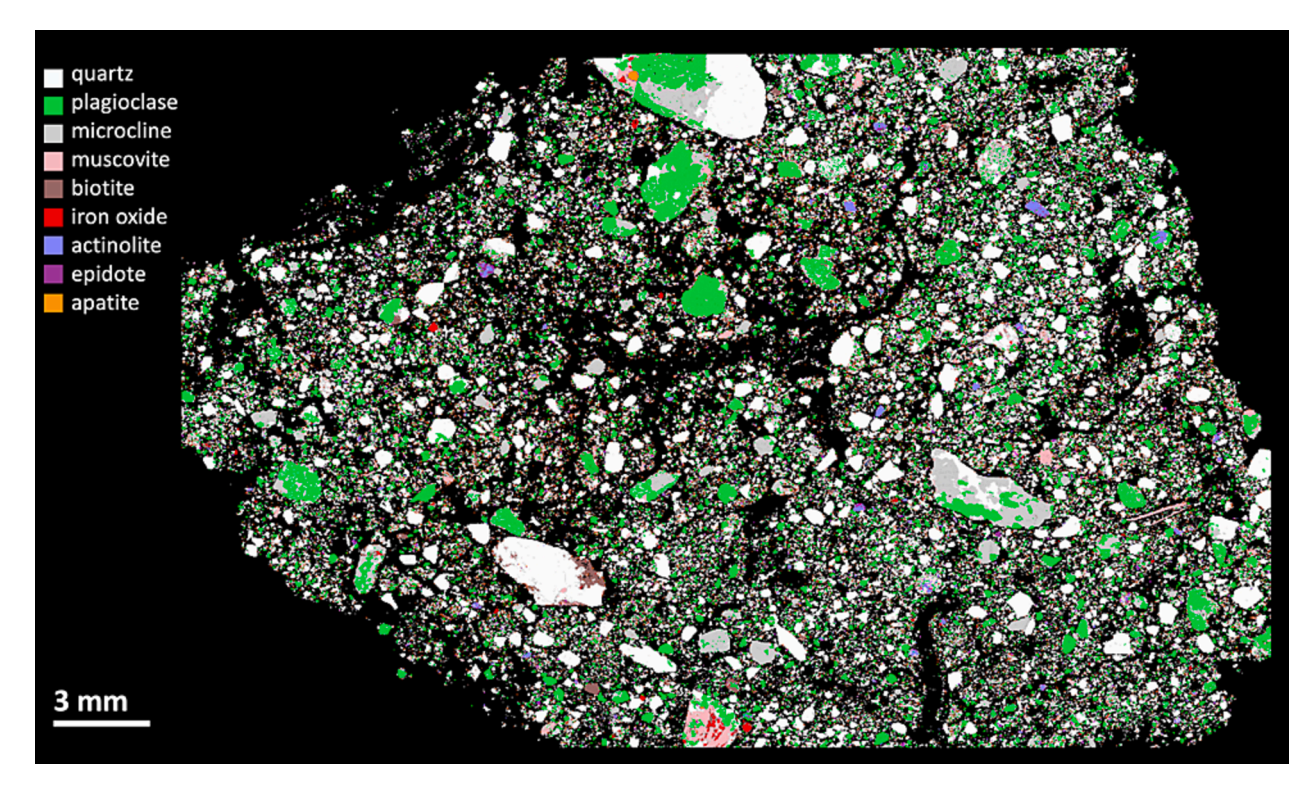


Fig. 7. Results of cluster-based EPMA mineralogical identification for a Bs horizon from a Typical podzol. Major mineral phases are given in the key. Black pixels represent voids.

Table 2 EPMA-determined abundance, in weight %, of the six most common minerals in soils of this study, organized by horizon and pit for 26 thin sections. Together, these six minerals make up \sim 98.8 % of the identified mineral matter. Quartz-based plagioclase depletion (calculated from EPMA data alone) is presented in the last column.

Pedon	Soil unit	Horizon	Quartz	Plagioclase	Microcline	Muscovite	Biotite/Chlorite	Actinolite
A1	E podzol	E	72.60 %	12.50 %	11.00 %	2.30 %	0.20 %	0.80 %
A2	Bhs podzol	Bhs	49.70 %	10.00 %	7.40 %	18.50 %	11.30 %	1.10 %
A2	Bhs podzol	Bhs	56.90 %	14.10 %	8.40 %	7.00 %	9.30 %	2.20 %
A2	Bhs podzol	BC	61.30 %	17.30 %	11.50 %	2.80 %	2.90 %	1.80 %
A3	Typical podzol	E	65.30 %	17.00 %	14.10 %	1.80 %	0.10 %	0.50 %
A3	Typical podzol	Bhs	61.30 %	18.10 %	13.70 %	3.00 %	0.50 %	1.10 %
A3	Typical podzol	Bh	56.90 %	20.50 %	14.50 %	3.20 %	1.00 %	2.30 %
B1	E podzol	E	70.40 %	9.30 %	16.60 %	2.90 %	0.20 %	0.20 %
B2	Bhs podzol	E	63.10 %	14.70 %	17.50 %	4.30 %	0.00 %	0.10 %
B2	Bhs podzol	Bhs	57.50 %	16.90 %	10.40 %	1.80 %	11.30 %	1.80 %
B2	Bhs podzol	Bhs	50.50 %	21.90 %	11.50 %	2.50 %	9.80 %	1.90 %
B2	Bhs podzol	BC	49.00 %	27.40 %	15.10 %	3.30 %	1.60 %	1.60 %
В3	Typical podzol	E	74.30 %	12.60 %	10.90 %	1.20 %	0.00 %	0.30 %
В3	Typical podzol	Bhs	65.30 %	16.70 %	13.40 %	2.10 %	0.30 %	0.70 %
В3	Typical podzol	Bs	62.90 %	20.30 %	11.50 %	2.30 %	1.00 %	1.20 %
C1	E podzol	E	64.80 %	13.90 %	15.50 %	4.90 %	0.20 %	0.30 %
C2	Bhs podzol	Bhs	39.60 %	22.10 %	10.70 %	11.90 %	12.80 %	2.60 %
C2	Bhs podzol	Bhs	59.60 %	18.60 %	12.90 %	2.70 %	1.90 %	1.60 %
C3	Typical podzol	E	70.20 %	13.40 %	13.10 %	1.90 %	0.00 %	0.40 %
C3	Typical podzol	Bhs	67.70 %	19.00 %	9.10 %	2.30 %	0.40 %	0.80 %
C3	Typical podzol	Bs	53.00 %	24.70 %	15.30 %	3.50 %	0.90 %	1.40 %
C3	Typical podzol	BC	50.10 %	24.80 %	17.90 %	2.60 %	1.50 %	2.10 %
A3	Typical podzol	C	45.10 %	30.70 %	18.30 %	2.50 %	0.90 %	1.50 %
AD	Drilled well	C	43.10 %	31.90 %	17.50 %	3.40 %	1.80 %	1.10 %
BD	Drilled well	C	41.00 %	37.20 %	15.30 %	3.30 %	1.00 %	1.50 %
CD	Drilled well	С	43.60 %	27.60 %	19.10 %	4.40 %	1.70 %	1.80 %

 τ values to the base of the solum of -0.74 and -0.73, respectively, compared with -0.56 and -0.54 in Bhs podzols and -0.40 and -0.41 in Typical podzols. Aluminum losses differed in magnitude from Na and Ca, reflecting the influence of pedogenic Al, but exhibited a similar pattern, with a median depth-integrated τ of -0.61 for E podzols, -0.34 for Bhs podzols, and -0.28 for Typical podzols. Differences of median τ between E podzols and Typical podzols were determined to be

significant for all three elements (p < 0.005; Fig. 3). Differences in medians between E podzols and Bhs podzols were significant in the case of τ_{Al} (p = 0.016; Fig. 3).

3.2. Micromorphological features

Micromorphological assessment of mineral alteration in soil clods

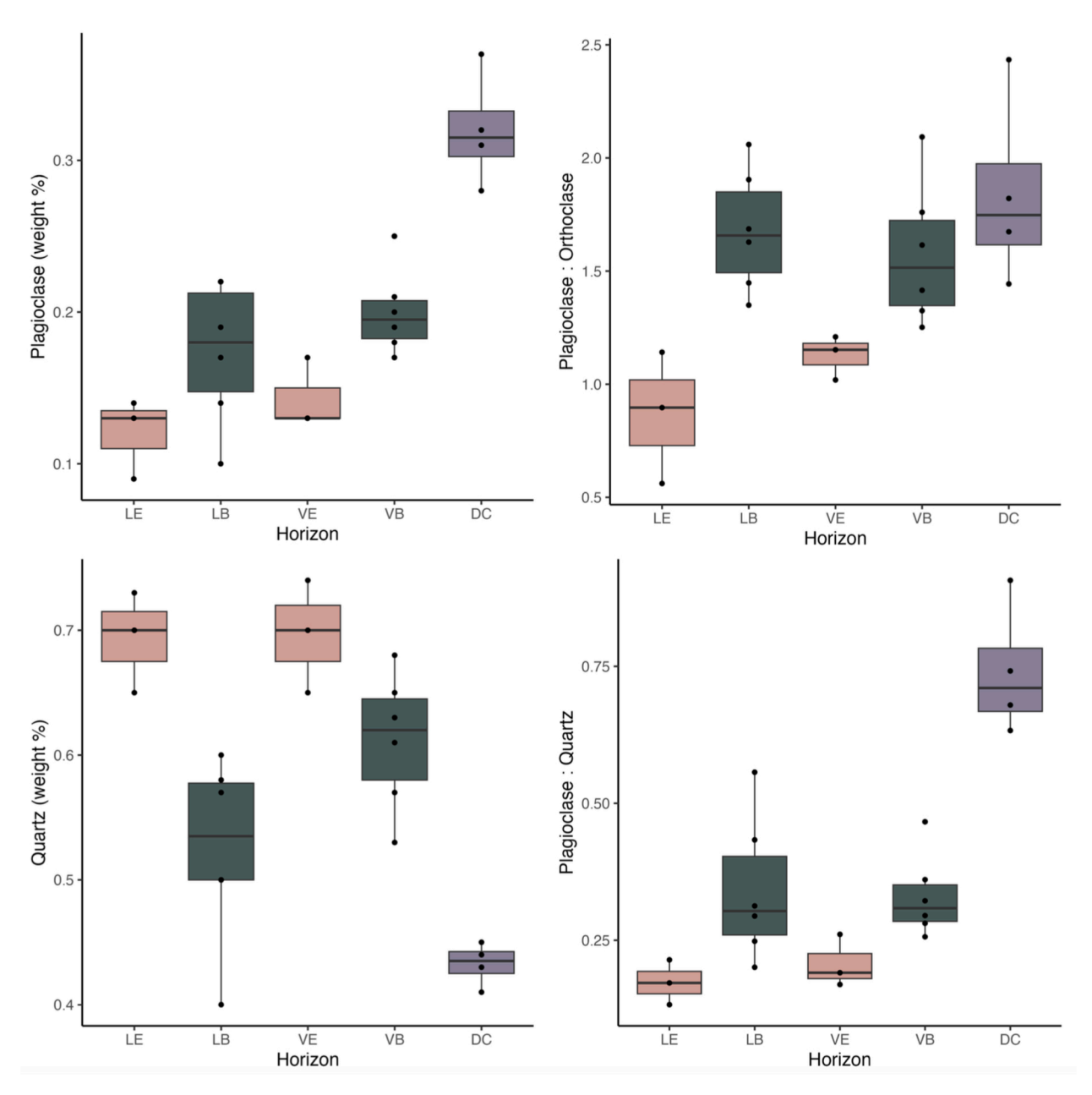


Fig. 8. EPMA-derived mineral abundances and mineral ratios for the three most common soil minerals (plagioclase, quartz, orthoclase), compared among genetic horizons. Mineral abundances are given in weight %, and bars represent standard errors. LE = lateral E horizon (from E podzols); LB = lateral B horizon (from Bhs podzols); VE = vertical E horizon (from Typical podzols); VB = vertical B horizon (Typical podzols); DC = deep C horizon (samples >100 cm from Bhs podzol and Typical podzol soil pits).

from the A transect showed plagioclase grains in the E horizon of the E podzol had the highest average degree of alteration (0.97 on a scale of 0-4, with 4 representing complete dissolution), followed by the Typical podzol E horizon (0.80), Typical podzol Bhs horizon (0.74), BC horizon of the Bhs podzol (0.66), Bhs horizon of the Bhs podzol (0.56), and finally C horizon had the lowest average degree of alteration (0.11). All plagioclase alteration appeared to be isomorphous, preserving the original shape and size of the mineral, and most of the alteration showed an irregular linear pattern, following the terminology of Stoops et al. (1979).

Three main patterns of weathering were observed in plagioclase grains: hyphal tunneling, pitting, and porosity around the grain boundaries of inclusions (Fig. 6). Tunneling morphology was consistent with hyphal features (Jongmans et al., 1997; Leyval and Berthelin, 1991), with tunnels showing a constant diameter and rounded end

(Fig. 6a). Tunneling was observed in all three soils of the A transect but was most common in the E podzol. We observed increased microporosity within plagioclase grains containing small inclusions of other minerals in soil clods of solum horizons. We also observed increased microporosity around grain boundaries of sericite (fine white micas) from sericitization of plagioclase during hydrothermal alteration (Fig. 6d), quartz from myrmekite (worm-like intergrowths) (Fig. 6c), and microcline (potassium feldspar) in perthite (a rock texture involving intergrowth of sodic alkali and potassium feldspars; Fig. A1). Sericite and myrmekite inclusions were present in plagioclase grains of all three soils regardless of depth. However, in plagioclase grains of C horizon thin sections, these features lacked the accompanying grain boundary microporosity found in solum plagioclase grains.

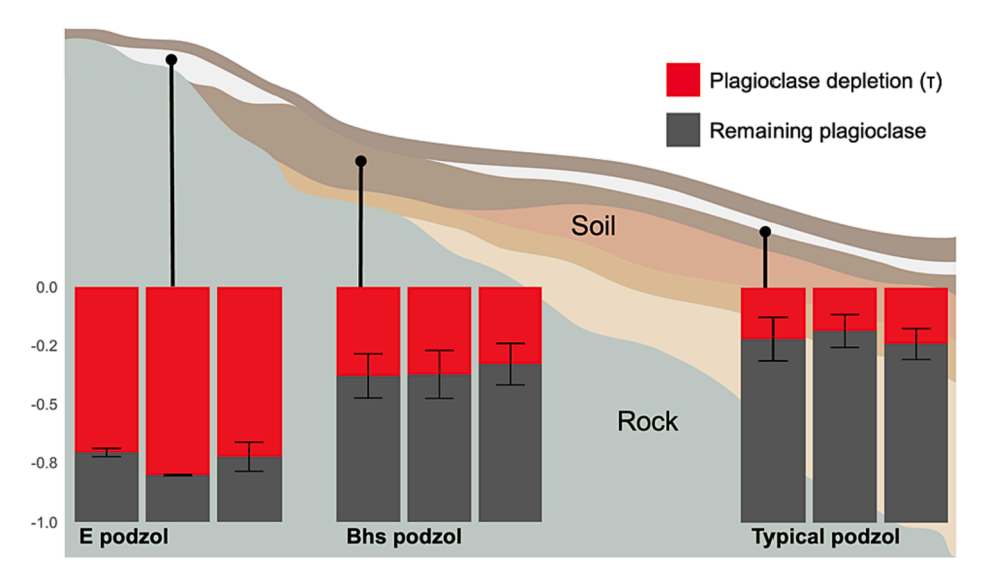


Fig. 9. Representation of plagioclase depletion in the nine pits studied at three locations along the hillslope. Note the y axis, which represents τ , with 0 representing no net loss of plagioclase, and -1 representing total loss of plagioclase. Red bars show whole-pedon (excluding BC and C horizons) plagioclase depletion. Gray bars represent remaining plagioclase. EPMA-derived estimates of plagioclase content per horizon were used to estimate the fraction of total Na bound in plagioclase. Plagioclase depletion was then calculated from total elemental data with Ti as an index element. Sample sizes for the number of horizons included within each integrated pit value are as follows, from right to left. E podzols: n = 4; n = 3; n = 2; Bhs podzols: n = 6; n = 5; n = 6; Typical podzols: n = 6; n = 5; n = 5.

3.3. Microprobe-based mineralogical and elemental quantification

An example of a thin section microphotograph and associated cluster-based EPMA mineralogical analysis is shown in Fig. 7. Considering soil heterogeneity and the small sample volume of intact soil clods, EPMA is not an appropriate method for estimating the total elemental concentration of soil horizons. Still, using the stoichiometry determined by SEM-EDS, we found that total Ca and Na calculated by EPMA were not unlike the results of total elemental digestion, with mean differences of 12 % and 10 %, respectively. These differences were not systematic. Average concentrations of relatively high-solubility minerals were higher in C horizons than solum horizons as expected, with plagioclase, actinolite, and apatite showing the largest reductions in concentration compared to C horizons. Quartz was the major mineral phase in all soils, followed by plagioclase, orthoclase, muscovite, biotite/chlorite, actinolite, iron oxide, epidote, almandine, and others (Table 2). Plagioclase concentrations ranged from 9 % to 37 % (wt. %) within identified material, with an average of 18 % for solum horizons and 32 % for C horizons. Plagioclase was the second most common mineral in 23 out of 26 soil thin sections, after quartz, and was third following microcline in the remaining 3 thin sections, which were eluvial horizons of laterally developed soils.

Quartz and plagioclase showed opposite trends with depth, with plagioclase concentrations decreasing and quartz concentrations increasing toward the soil surface (Fig. 8). The average ratio of plagioclase to quartz and plagioclase to orthoclase was lowest in E horizons of E podzols, followed, in increasing order, by E horizons of Typical podzols, Bhs horizons of Typical podzols, Bhs horizons in Bhs podzols, and C horizons (Fig. 8). Mass losses of plagioclase ($\tau_{\text{plagioclase}}$), calculated using quartz as a reference element, showed similar depletion values to Tibased τ_{Na} (Fig. A2). A positive linear relationship was observed between $\tau_{plagioclase}$ and $\tau_{Na},$ with Spearman's rank correlation coefficient of 0.65 (p < 0.001). Estimated losses for E horizons of E podzols were highly correlated, with τ differing by less than 5 %, while Bhs horizons were the least correlated. Despite the close spacing of soils in each transect (84-163 m), Ti-based plagioclase losses differed significantly when comparing whole profiles (Fig. 9). Whole profile Ti-based estimates of $\tau_{plagioclase}$ differed by podzol type and followed similar patterns to depth-weighted mean τ_{Na} values presented in the previous section. Close to three-quarters of the plagioclase in the original mineral pool of E podzols has been lost since deposition (mean of 3 pits = -0.74), compared to under half for Bhs podzols (mean of 3 pits = -0.39) and around a quarter for Typical podzols (mean of 3 pits = -0.23).

4. Discussion

4.1. Elemental patterns

The elemental trends exhibited by soils organized along a catena in this study reveal a spatial ordering of chemical weathering that is strongly linked to soil morphology, which has formed as a function of the hydrologic regime created by topographic position and depth to bedrock. The strongest patterns within τ and total elemental concentration were observed in the case of Na (Table 1; Figs. 3 and 5). Trends in Ca and Al were less significant, reflecting the influence of nonplagioclase reservoirs for these elements. Ca is found in a range of common primary minerals (albeit in lower abundance compared to plagioclase), secondary non-crystalline phases (Bel et al., 2020), cation exchange complexes, and is actively biocycled. Al is a major component of common abundant primary minerals, secondary non-crystalline phases, and cation exchange complexes. Sodium has been used as a proxy to study plagioclase weathering in granitic terrains because it doesn't bioaccumulate significantly in soil and there are few other Nabearing minerals of high abundance (Rasmussen et al., 2011), which was confirmed for this study.

The significant differences in τ observed for Na between laterally developed E horizons and vertically developed E horizons at similar depths of soils only 100 m apart suggest that eluviation, and therefore pedogenesis, does not proceed uniformly within soils along the hillslope (Table 1; Fig. 5). The absence of a significant difference between τ_{Na} and τ_{Ca} of vertical E and vertical Bhs horizons (Fig. 5) is surprising, given the eluviation involved in podzolization. Greater differences between these horizons were observed for quartz-based $\tau_{plagioclase}$ than Ti-based τ_{Na} and τ_{Ca} . When E horizons were present above Bhs horizons, Ti concentrations were often slightly enriched in Bhs horizons relative to overlying E horizons, a phenomenon observed for seven out of the nine Bhs and Typical podzols, which may indicate minor translocation of Ti. Because Ti is only one component of the ratio used to calculate fractional mass loss, this enrichment resulted in a more negative τ in Bhs horizons relative to E horizons within four of the nine Bhs and Typical podzols. It

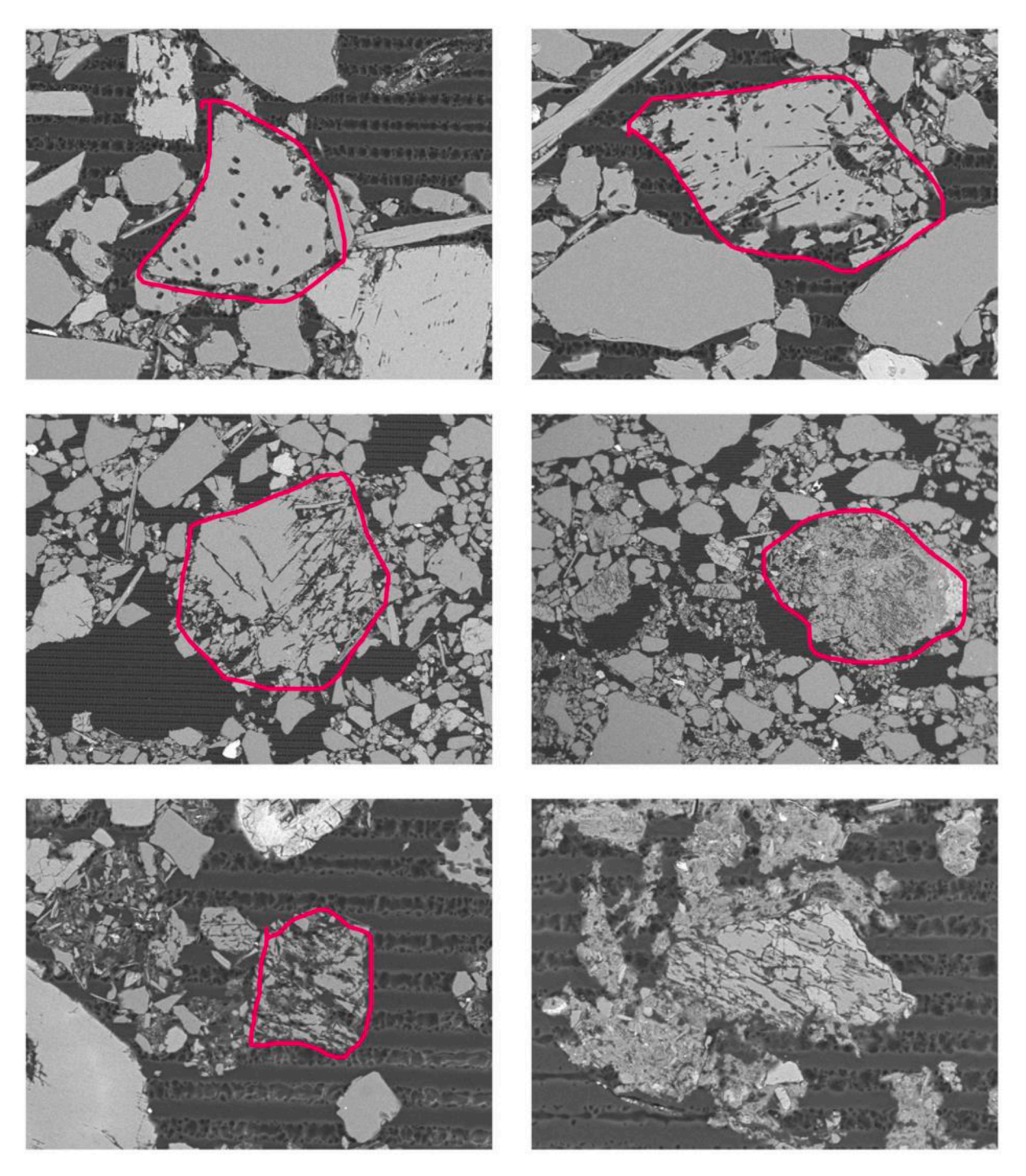


Fig. A1. Images depicting the scale used to help assess alteration in plagioclase grains, and as one microfeature not included in the main body of the article. The alteration grades are given as follows. Upper left: 0.5; upper right: 1; middle left: 1.5; middle right: 2; bottom left; 2.5. Bottom right: grain of perthite showing intergrowth of potassium and sodic feldspars.

is possible that the hypothesized slight translocation of Ti from E to Bhs horizons could deflate the magnitude of the difference in estimated τ_{Na} and τ_{Ca} between these horizons. This likely would not influence the comparison between E horizons of E podzol and Typical podzols, assuming Ti translocation operates uniformly in the landscape, an assumption that is discussed in more detail in Appendix A. Our finding that quartz-based $\tau_{plagioclase}$ and Ti-based τ_{Na} were positively correlated at r=0.65~(p<0.001) is low (Fig. A2), given that the samples were collected from the same horizons. This is likely due to random variation given the magnitude of the 2D mineral area surveyed by the soil thin sections (~12.5 cm²) in comparison to the 3D volume submitted for

total elemental analysis ($\sim 20 \text{ cm}^3$).

The range of τ_{Na} observed in this study is in the same range as other estimates of τ_{Na} in podzols at HBEF (Nezat et al., 2004) and elsewhere in the Northeastern USA (Jersak et al., 1995). Despite losses, an average of 51 % of the Na and Ca remains in mineral horizons of E podzols compared to the Na and Ca content of the parent material (C horizon). Less than 2 % of this resides in the exchangeable fraction, and organic matter in these soils is low, revealing that the remaining mineral content still constitutes a significant base cation pool. The size of the remaining mineral pool might appear to contradict our finding that 71 % of Na and Ca is depleted according to τ , which is explained by examining the

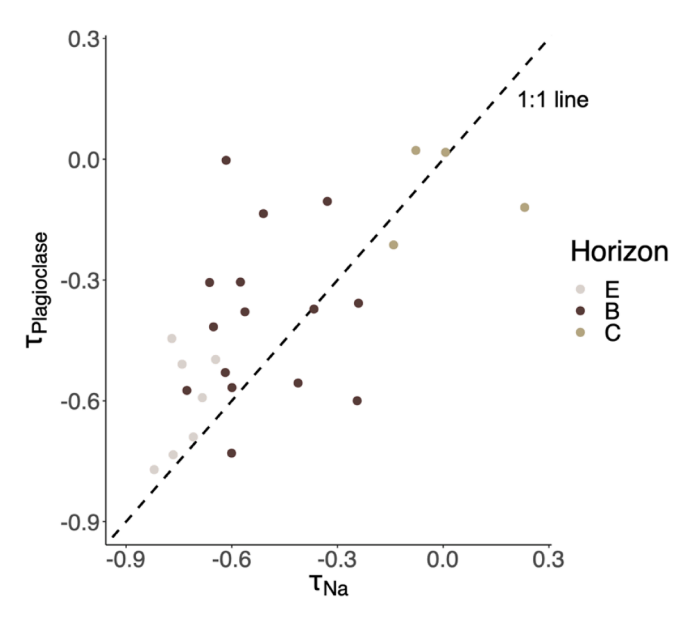


Fig. A2. Quartz-based plagioclase depletion vs. Ti-based Na depletion. The dotted line is a 1:1 line where points would be expected to fall given total agreement. Despite the difference in methods and despite the methods being based on plagioclase and Na, respectively, a positive linear relationship was observed, with a Spearman's rank correlation coefficient of 0.65 (p < 0.001; regression not shown).

fractional mass loss approach. As described in our methods, the mass loss approach measures weathering by expanding the comparison of soil to parent material using index constituents, which are enriched in the soil as other materials weather. Therefore, τ shows the depletion of the element of interest relative to this index element. In this case, the progression of congruent weathering reactions led to higher depletion values using τ than those attained by comparing Ca and Na in soil to Ca and Na in parent material through a simple ratio. This reflects the concentration of the index element over time, as Ca and Na dissolve and leave Ti behind.

4.2. Microscale weathering

In addition to the type and chemical composition of minerals present, the micromorphological investigation revealed mineralogical features that influence weathering susceptibility. Plagioclase inclusions represent an important microfeature due to the potential priming effect of inclusions on weathering. The boundaries (separation planes) of these inclusions create areas of mechanical weakness and are important for the development of intramineral porosity and subsequent internal weathering (Delvigne, 1998; Stoops et al., 1979). Sericite and myrmekite inclusions observed in plagioclase are probably derived from the main till source lithology, Kinsman granodiorite (Barker, 1961). Due to its prevalence and the small size of sericite grains, sericitization is expected to have enhanced the expansion of porosity within plagioclase through the formation of microporosity along grain boundaries. These features illustrate how parent material properties can potentially affect pedogenesis and soil weathering at the microscale, not just through macroscale properties such as hydraulic conductivity and bulk

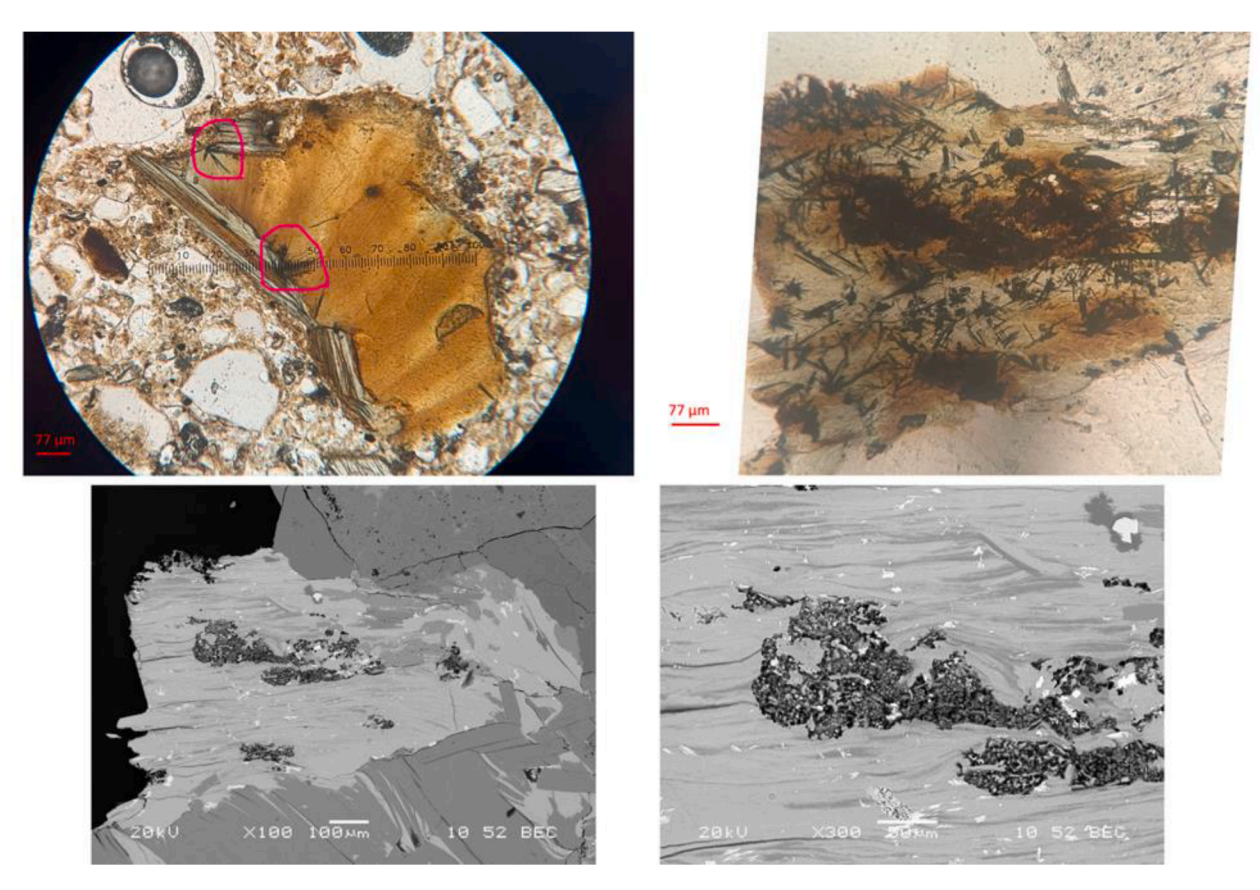


Fig. A3. Example microphotographs of sagenitic biotite and chlorite grains. The image in the upper left is a biotite grain with chlorite intergrowths collected from the BC horizon of a Bhs podzol. Sagenite inclusions are circled and are black in color with a needle-like (acicular) habit. At the upper right is a close-up view of a biotite/chlorite grain from a soil-embedded rock fragment of Kinsman granodiorite, which is the major contributing till lithology. Sagenite, likely composed of rutile and/or titanite, is once again black and acicular. The same grain is shown via SEM microphotograph in the lower two microphotographs, collected at different resolutions. In this view, the inclusions appear much smaller because of the large spot size and low depth of field.

Table A1 Full τ , extractable ion, and carbon information for horizons analyzed. Values of τ differ slightly from the values presented in the main body because the main body table was calculated from raw data, whereas the values presented in this table were calculated from the values adjusted for significant figures.

Pedon	Horizon	FieldName	pН	C (%)	Ca (cmol kg ⁻¹)	Na (cmol kg ⁻¹)	Al (cmol kg ⁻¹)	Ti/(Ti + Zr)	Ti (mg kg ⁻¹)	τAl	τСа	τNa
A1_Well	E1	42_2_PFM_E1	3.3	5.5	0.03	0.02	1.82	0.93	5100	-0.63	-0.75	-0.76
A1_Well	E2	42_2_PFM_E2	3.6	0.64	0.01	0.01	0.59	0.92	2970	-0.39	-0.4	-0.49
A1	A	42_2_V2.1_A	NA	10.2	0.36	0.1	0.38	0.94	3240	-0.59	-0.67	-0.7
A1	E.1	42_2_V2.1_E.1	3.2	1.15	0.04	0.01	0.59	0.93	5010	-0.63	-0.78	-0.73
A1	E.2	42_2_V2.1_E.2	3.4	0.94	0.01	0.01	1.2	0.93	5180	-0.63	-0.8	-0.74
A1	E.3	42_2_V2.1_E.3	3.4	0.69	0.01	0.01	1.54	0.93	5300	-0.64	-0.78	-0.76
A1	E.4	42_2_V2.1_E.4	4.5	0.5	0.01	0.01	1.12	0.92	4140	-0.59	-0.71	-0.69
A2_Well	A	42_3_PFM_A	NA	16.9	0.36	0.07	2.45	0.93	2270	-0.39	-0.5	-0.55
A2_Well	Bhs1	42_3_PFM_Bhs1	3.7	5.69	0.04	0.01	3.06	0.93	3170	-0.39	-0.52	-0.57
A2_Well A2_Well	Bhs2 Bhs3	42_3_PFM_Bhs2 42_3_PFM_Bhs3	3.8 3.9	4.56 5.08	0.03 0.05	0.01 0.02	3.99 4.29	0.92 0.93	3570 3400	-0.38 -0.33	-0.59 -0.55	$-0.6 \\ -0.6$
A2_weii A2	Oa	42_3_PFW_BIIS3 42_3_V3.1_Oa	NA	24.7	NA	NA	NA	0.95	1850	-0.33 -0.37	-0.55 -0.61	-0.63
A2	Bhs1	42_3_V3.1_Bhs1	3.7	4.88	0.03	0.02	1.56	0.93	3640	-0.47	-0.63	-0.6
A2	Bhs2.1	42 3 V3.1 Bhs2.1	4.1	3.83	0.04	0.01	3.28	0.93	3970	-0.48	-0.67	-0.65
A2	Bhs2.2	42_3_V3.1_Bhs2.2	NA	5.02	0.05	0.01	4.34	0.95	3100	-0.24	-0.47	-0.5
A2	Bhs3.1	42_3_V3.1_Bhs3.1	4.4	4.28	0.04	0.01	4.35	0.94	2730	-0.13	-0.34	-0.37
A2	Bhs3.2	42_3_V3.1_Bhs3.2	4.3	3.37	0.03	0.01	3	0.92	2840	-0.17	-0.26	-0.32
A2	Bhs3.3	42_3_V3.1_Bhs3.3	4.2	2.67	0.03	0.01	2.6	0.92	2750	-0.13	-0.13	-0.23
A2	BC.1	42_3_V3.1_BC.1	4.3	1.99	0.03	0.01	2.41	0.94	2340	0.02	-0.01	-0.02
A2	BC.2	42_3_V3.1_BC.2	4.3	1.86	0.03	0.01	2.51	0.91	2370	0	0.03	-0.05
A2	BC.3	42_3_V3.1_BC.3	4.3	1.13	0.01	0	1.84	0.92	2310	0.07	0.1	0.07
A2	D.2	42_3_V3.1_D.2	4.3	0.4	0.01	0.01	2.05	0.94	2780	0.02	0.07	-0.04
A2 A3 Well	D.10	42_3_V3.1_D.10 42 4 PFM E	NA	0.21	0.05	0.04	2.02	0.95	2680	0.02	-0.08	-0.05
A3_Well	E Bhs1	42_4_PFM_E 42_4_PFM_Bhs1	3.1 3.2	2.36 6.59	0.15 0.12	0.02 0.05	0.34 2.81	0.93 0.95	3130 3400	-0.38 -0.45	-0.49 -0.54	-0.45 -0.56
A3_Well	Bhs2	42_4_PFM_Bhs2	3.6	5.52	0.12	0.02	5.04	0.93	3420	-0.43	-0.54	-0.36
A3_Well	Bh	42_4_PFM_Bh	4.1	3.15	0.05	0.01	3.41	0.93	2630	-0.08	-0.14	-0.25
A3_Well	BC	42_4_PFM_BC	4.2	3.14	0.04	0.01	2.42	0.92	2400	-0.01	0.03	-0.13
A3	Α	42_4_V4.1_A	2.6	18.9	2.44	0.03	0.21	0.95	1540	-0.34	-0.36	-0.44
A3	E	42_4_V4.1_E	3.1	1.37	0.1	0.01	0.41	0.93	3380	-0.4	-0.62	-0.5
A3	Bhs1	42_4_V4.1_Bhs1	3.3	2.83	0.14	0.01	2.48	0.95	3930	-0.47	-0.64	-0.57
A3	Bhs2.1	42_4_V4.1_Bhs2.1	3.5	4.56	0.13	0.02	3.77	0.95	3060	-0.28	-0.51	-0.41
A3	Bhs2.2	42_4_V4.1_Bhs2.2	3.7	4.79	0.12	0.02	3.74	0.93	2710	-0.24	-0.38	-0.35
A3	Bh.1	42_4_V4.1_Bh.1	3.9	4.37	0.08	0.01	5.89	0.93	2400	-0.01	-0.19	-0.18
A3	Bh.2	42_4_V4.1_Bh.2	4	3.75	0.04	0.01	5.36	0.92	2380	0.08	-0.11	-0.09
A3	BC	42_4_V4.1_BC	4.2	2.08	0.03	0.01	5.48	0.92	2370	0.11	-0.08	0.03
A3	C.2	42_4_V4.1_C.2	NA	0.36	0.01 0.03	0.01 0.01	1.69 1.03	0.92 0.91	2480 2370	0.01 0.09	0.05	0.02
A3 A3	D.4 D.9	42_4_V4.1_D.4 42_4_V4.1_D.9	4.4 NA	0.2 0.17	NA	NA	NA	0.91	1880	0.09	0.1 0.18	0.15 0.38
B1_Well	Oa	52_2_PFM_Oa	NA	31.2	NA NA	NA NA	NA NA	0.98	893	-0.39	-0.54	-0.7
B1_Well	E	52_2_FFM_E	3.2	2.72	0.11	0.02	1.64	0.94	5560	-0.59	-0.82	-0.77
B1	Oa	52_2_X2.1_Oa	NA	25.1	NA	NA	NA	0.96	3040	-0.63	-0.87	-0.83
B1	E1.1	52_2_X2.1_E1.1	3.3	1.91	0.03	0.01	0.73	0.93	5530	-0.64	-0.87	-0.78
B1	E1.2	52_2_X2.1_E1.2	3.4	1.09	0.03	0.01	0.82	0.93	4680	-0.62	-0.86	-0.77
B1	E2	52_2_X2.1_E2	3.4	0.44	0.02	0	0.74	0.93	4690	-0.64	-0.85	-0.77
B2_Well	Oa	52_3_PFM_Oa	NA	20.2	0.23	0.16	3.45	0.95	2940	-0.5	-0.67	-0.69
B2_Well	Bhs1	52_3_PFM_Bhs1	3.2	8.37	0.11	0.04	1.99	0.94	4290	-0.55	-0.72	-0.7
B2_Well	Bhs2	52_3_PFM_Bhs2	3.8	1.66	0.06	0.01	1.15	0.92	4210	-0.51	-0.51	-0.58
B2	A	52_3_X3.1_A	2.9	11.2	0.35	0.03	0.77	0.92	2940	-0.43	-0.63	-0.55
B2	E	52_3_X3.1_E	3.3	1.85	0.04	0.01 0.02	1	0.91	3960	-0.49	-0.68	-0.59
B2 B2	Bhs1 Bhs2.1	52_3_X3.1_Bhs1 52_3_X3.1_Bhs2.1	3.5 3.7	8.57 6.54	0.09 0.07	0.02	5.14 4.86	0.95 0.93	4380 3630	-0.59 -0.49	-0.71 -0.63	-0.73 -0.64
B2	Bhs2.1	52_3_X3.1_Bhs2.2	3.8	6.54	0.05	0.03	4.61	0.93	3700	-0.49 -0.4	-0.03	-0.56
B2	Bhs2.3	52_3_X3.1_Bhs2.3	4	4.68	0.05	0.03	7.65	0.93	3480	-0.4	-0.35	-0.30
B2	BC.1	52_3_X3.1_BC.1	4.2	2.48	0.03	0.01	5.82	0.92	3240	-0.17	-0.26	-0.27
B2	BC.2	52_3_X3.1_BC.2	4.3	1.15	0.02	0	4.34	0.91	3650	-0.32	-0.23	-0.36
B2	D.1	52_3_X3.1_D.1	4.8	0.27	0.34	0.09	1.04	0.94	2870	-0.03	-0.12	-0.07
B2	D.2	52_3_X3.1_D.2	NA	NA	NA	NA	NA	0.96	4000	-0.19	-0.38	-0.43
B2	D.3	52_3_X3.1_D.3	4.8	0.05	0.22	0.04	0.13	0.95	2150	0.07	0.03	0.08
В3	A	52_4_X4.1_A	2.8	11.5	0.16	0.04	0.3	0.91	2590	-0.43	-0.57	-0.49
В3	E	52_4_X4.1_E	3.3	0.98	0.03	0.01	0.79	0.92	2970	-0.37	-0.6	-0.45
B3	Bhs	52_4_X4.1_Bhs	3.5	5.25	0.06	0.02	4.08	0.95	2980	-0.34	-0.52	-0.42
B3	Bs1	52_4_X4.1_Bs1	3.8	4.67	0.06	0.02	5.76	0.92	2820	-0.25	-0.43	-0.38
B3 B3	Bs2.1 Bs2.2	52_4_X4.1_Bs2.1	4	5.91 5.01	0.06	0.01	6.8	0.94 0.92	2260	$0 \\ -0.09$	$-0.3 \\ -0.27$	$-0.21 \\ -0.28$
B3	BS2.2 BC.1	52_4_X4.1_Bs2.2 52_4_X4.1_BC.1	4.1 4.3	2.58	0.05 0.03	0.01 0.01	6.04 4.47	0.92	2480 2470	-0.09 -0.01	-0.27 -0.19	-0.28 -0.14
В3	BC.1 BC.2	52_4_X4.1_BC.1 52_4_X4.1_BC.2	4.3 4.4	2.34	0.03	0.01	4.47	0.92	2590	-0.01 -0.05	-0.19 -0.23	-0.14 -0.17
B3	D.3	52_4_X4.1_D.3	4.5	0.43	0.02	0.01	1.55	0.93	1830	0.18	0.25	0.19
B3	D.6	52_4_X4.1_D.6	4.6	0.33	0.02	0.01	1.48	0.95	1350	0.5	0.46	0.59
В3	D.8	52_4_X4.1_D.8	4.5	0.28	0.03	0.01	4.71	0.93	1410	0.51	0.36	0.65
В3	D.9	52_4_X4.1_D.9	4.6	0.15	0.03	0.01	0.96	0.91	2520	-0.02	0.17	0.08
В3	D.16	52_4_X4.1_D.16	4.9	0.05	0.84	0.04	0.15	0.92	2880	-0.09	0.02	-0.04
C1_Well	Oa	86_2_PFM_Oa	NA	30.1	1.59	0.06	0.5	0.99	1060	-0.54	-0.59	-0.73

(continued on next page)

Table A1 (continued)

Pedon	Horizon	FieldName	pН	C (%)	Ca (cmol kg ⁻¹)	Na (cmol kg ⁻¹)	Al (cmol kg ⁻¹)	Ti/(Ti + Zr)	Ti (mg kg ⁻¹)	τAl	τCa	τNa
C1_Well	E	86_2_PFM_E	NA	0.48	0.03	0.01	0.21	0.9	3070	-0.46	-0.5	-0.57
C1	Oa	86_2_W2.2_Oa	NA	34	2.84	0.1	1.4	0.99	222	0.13	0.78	-0.47
C1	E.1	86_2_W2.2_E.1	3.6	0.66	0.02	0.01	2.08	0.95	5130	-0.59	-0.67	-0.69
C1	E.2	86_2_W2.2_E.2	3.6	0.72	0.03	0	2.26	0.96	7090	-0.72	-0.69	-0.8
C2_Well	Oa	86_3_PFM_Oa	3.2	25.5	0.3	0.05	8.63	0.97	641	0.63	-0.54	-0.61
C2_Well	Bhs1	86_3_PFM_Bhs1	NA	17.8	0.25	0.06	13.1	0.95	1570	0.07	-0.54	-0.57
C2_Well	Bhs2	86_3_PFM_Bhs2	3.9	6.28	0.12	0.02	7.55	0.94	3630	-0.37	-0.55	-0.54
C2_Well	C	86_3_PFM_C	4	1.24	0.04	0.01	2.8	0.92	2680	-0.2	-0.09	-0.2
C2	Oa	86_3_W3.2_Oa	NA	32.8	2.91	0.09	1.19	0.98	557	-0.33	-0.12	-0.63
C2	A	86_3_W3.2_A	3.2	10.7	0.41	0.03	3.2	0.95	3800	-0.47	-0.59	-0.57
C2	Bhs1	86_3_W3.2_Bhs1	3.4	8.01	8.52	22.4	5.41	0.94	4270	-0.46	-0.63	-0.6
C2	Bhs2.1	86_3_W3.2_Bhs2.1	3.5	6	0.11	0.01	3.88	0.93	3550	-0.39	-0.52	-0.49
C2	Bhs2.2	86_3_W3.2_Bhs2.2	3.6	5.88	0.13	0.02	8	0.93	3470	-0.37	-0.51	-0.49
C2	Bhs3.1	86_3_W3.2_Bhs3.1	3.7	2.39	0.06	0.01	5.52	0.93	2700	-0.23	-0.33	-0.3
C2	Bhs3.2	86_3_W3.2_Bhs3.2	3.7	2.42	0.07	0.01	5.99	0.93	2820	-0.24	-0.36	-0.3
C3_Well	Oa	86_4_PFM_Oa	NA	24.7	1.22	0.06	3.68	0.95	647	0	-0.27	-0.6
C3_Well	E	86_4_PFM_E	3	1.26	0.21	0.01	0.35	0.92	3980	-0.55	-0.67	-0.61
C3_Well	Bhs	86_4_PFM_Bhs	3.2	7.91	0.39	0.02	3.4	0.95	3840	-0.52	-0.58	-0.6
C3_Well	Bs	86_4_PFM_Bs	3.9	6.1	0.12	0.01	9.08	0.94	3250	-0.28	-0.4	-0.49
C3_Well	BC	86_4_PFM_BC	3.9	5.12	0.12	0.03	9.75	0.95	4390	-0.42	-0.53	-0.58
C3	Oa	86_4_W4.1_Oa	2.8	28.6	4.24	0.05	0.43	0.96	863	-0.34	-0.13	-0.55
C3	E	86_4_W4.1_E	3	1.24	0.21	0.01	0.7	0.92	3440	-0.46	-0.62	-0.51
C3	Bhs	86_4_W4.1_Bhs	3.2	5.29	0.46	0.02	3.71	0.93	3870	-0.47	-0.54	-0.53
C3	Bs.1	86_4_W4.1_Bs.1	3.6	2.82	0.1	0.01	6.52	0.92	3350	-0.32	-0.36	-0.38
C3	Bs.2	86_4_W4.1_Bs.2	3.7	3.15	0.08	0.01	7.91	0.93	3150	-0.25	-0.35	-0.36
C3	Bs.3	86_4_W4.1_Bs.3	3.9	4.05	0.08	0.02	5.51	0.93	3070	-0.16	-0.36	-0.34
C3	BC.1	86_4_W4.1_BC.1	4	4	0.06	0.01	NA	0.93	3100	-0.11	-0.32	-0.3
C3	BC.2	86_4_W4.1_BC.2	4.1	2.69	0.05	0.01	13	0.92	3110	-0.17	-0.25	-0.23
C3	D.1	86_4_W4.1_D.1	4.2	1.47	0.05	0.01	14.2	0.92	2740	-0.06	-0.15	-0.1
C3	D.2	86_4_W4.1_D.2	4	1.24	0.06	0.01	11.9	0.92	2890	-0.16	-0.14	-0.16
C3	D.4	86_4_W4.1_D.4	4.2	0.59	0.03	0.01	8.59	0.92	2390	0.03	0.01	0.08
AD_Well	2	42_4_d1_2	NA	0.04	NA	NA	NA	0.92	2601	0.03	-0.05	0.02
BD_Well	3	52_4_d2_3	NA	0.04	NA	NA	NA	0.93	3141	-0.14	-0.01	-0.12
CD_Well	2	86_3_d2_2	NA	0.11	NA	NA	NA	0.93	2979	-0.07	-0.23	-0.21

mineralogy. The identification of similar inclusions in plagioclase grains throughout the three soils studied suggests that the weathering gradient we find is not attributable to variation in microscale weathering features, but instead due to differences in pedogenesis.

4.3. Mineralogical patterns

Along with the similarity in τ between Na and Ca, the correlation between τ_{Na} and $\tau_{plagioclase}$ indicates that plagioclase weathering is the principal reaction controlling the formation of a hillslope weathering gradient (Tables 1 and 2; Fig. A2). Our findings support the hypothesis by Likens et al. (1998) that plagioclase is the main mineral supplying Ca at HBEF (Table 2). Dominance of plagioclase in chemical weathering is a common finding in soils developed from granitic parent material in other contexts (Ferrier et al., 2010; Rasmussen et al., 2011; White et al., 2001).

The bulk soil mineralogy determined in this study agrees with other studies conducted at HBEF. Nezat et al. (2004) estimated 47 % quartz and 27 % plagioclase in parent material samples, close to this study's findings of 43 % quartz and 32 % plagioclase within identified material in parent material samples (Table 2). Actual plagioclase loss may be higher than EPMA-estimated plagioclase loss due to the presence of subpixel internal microporosity, such as mycorrhizal tunnels, which tend to be ~5 µm in diameter, and microporosity around mineral inclusions (Fig. 6). Because of the high Ca concentration of apatite, it was almost always well differentiated from other minerals. We found no free (not occluded within minerals) apatite in solum horizons. Only one mineral inclusion of apatite was identified in a solum horizon, a lower Bs horizon, which suggests that mineral inclusions of apatite do not persist significantly in the solum. This contradicts the assertion by Nezat et al. (2007) that 30 % of the original apatite in HBEF parent material remains in mineral inclusions of upper solum horizons. It is unlikely that apatite inclusions were overlooked with EPMA and unlikely that they would

also have been overlooked during our investigation with SEM-EDS. Because of the range in chemical compositions, certain minerals such as garnet species (almandine, grossular) were identified in SEM but difficult to quantify via EPMA. This led them to sometimes be classified into other mineral classes, such as chlorite and epidote. Overall, the sandy texture of HBEF soils gave a high accuracy of mineral identification, given that most particles were greater in size than the pixel resolution (30×30 μm). This allowed us to confirm the presence of a mineral weathering gradient at the microscopic scale and identify plagioclase as the dominant weathering mineral.

4.4. Ecological relevance

The plagioclase weathering gradient we observe is accompanied by patterns in vegetation and solution chemistry. Mixed coniferous vegetation, mosses, and lichens are frequently found in shallow bedrock soils in our study area. These are associated with lower pH and higher DOC concentrations in streamwater and soils of our study area, and in New England (Bailey et al., 2019a; Fakhraei and Driscoll, 2015; Johnson et al., 2000; LoRusso et al., 2021), in contrast to downslope soils which are dominated by deciduous species. The higher DOC and acidity associated with the coniferous vegetation area are expected to contribute to the enhanced weathering in shallow soils.

Our work has implications for mineral nutrition of plants at the pedon scale. Regionally, soil Ca was depleted by acid deposition in the decades prior to the passage of the Clean Air Act in the United States, which limited anthropogenic sources of strong acids in rain (Federer et al., 1989). The spatial nature of the plagioclase weathering gradient could influence the ongoing recovery of the plant-available and exchangeable Ca fractions. Notwithstanding the intensity of plagioclase depletion in soils at the upper end of the hillslope, it remains a dominant primary mineral in the soil. The remaining plagioclase contains Ca of local importance, especially to stationary organisms such as plants.

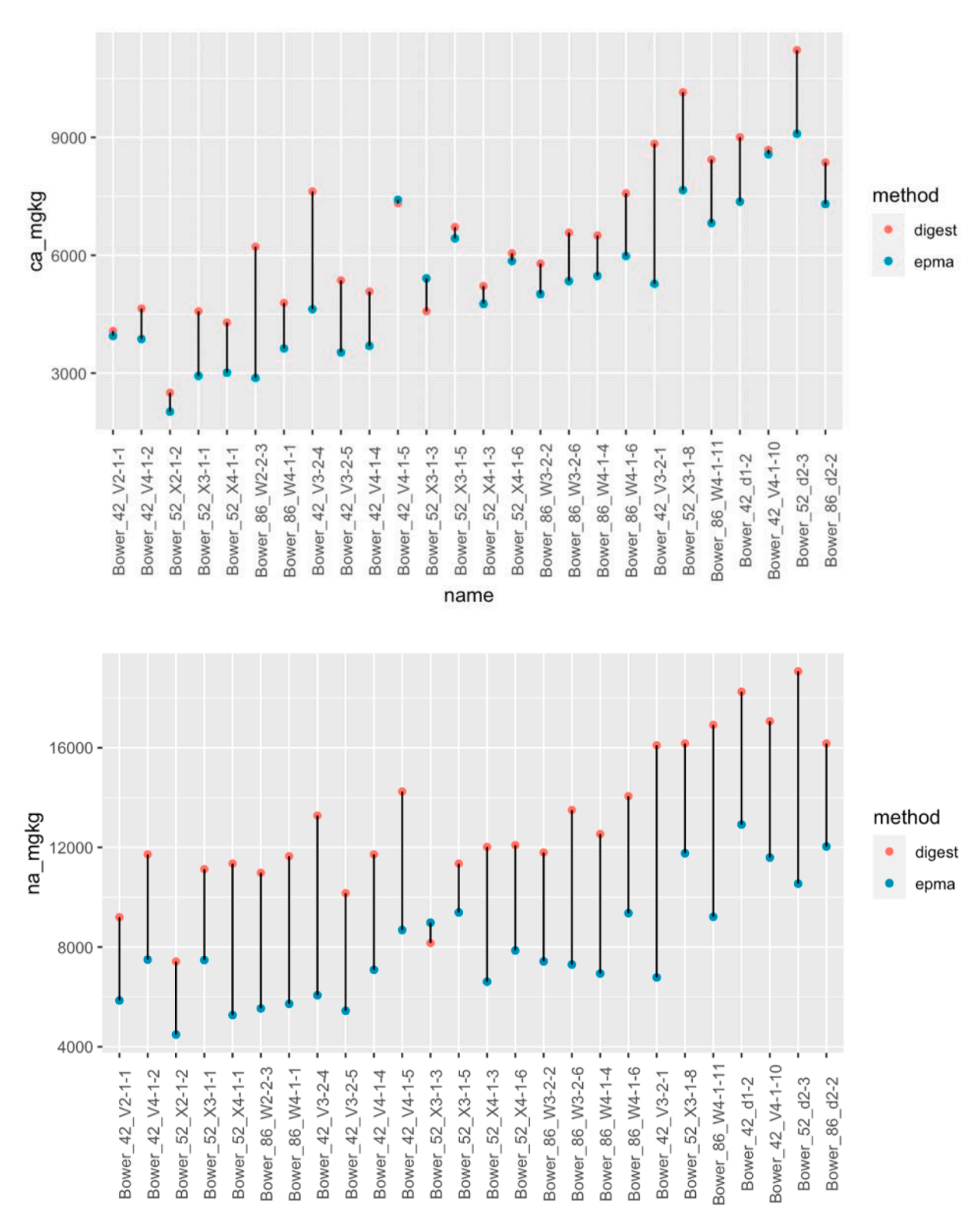


Fig. A4. Top: Divergence between Ca determined through elemental digestion vs. Ca determined through EPMA. Bottom: Divergence between Na determined through elemental digestion vs. Na estimated through EPMA. Note that elemental digestion involved analysis of \sim 20 mL volume of sample, whereas EPMA involved analysis of \sim 6 cm² of sample.

name

4.5. Pedogenic implications

The spatial patterning of weathering intensity observed in this study is reflective of soil properties organized by the intersecting influences of soil-forming factors and local hydrologic patterns. The gradient in

plagioclase dissolution (Table 2; Fig. 9) is highly related to contrasts in water table regimes and aqueous trends in DOC and acidity previously identified at Watershed 3 in HBEF (Bailey et al., 2019a; Benton et al., 2022; Gannon et al., 2014). Lateral water flow in E podzols and Bhs podzols is facilitated by the shallow depth to bedrock, proximity of

bedrock outcrops upslope, and low storage and infiltration. These soils experience saturation in the solum much more frequently than in Typical podzols, implying enhanced eluviation in E podzols and translocation of weathering products to Bhs podzols (Bailey et al., 2014). Gannon et al. (2015) determined that acidic DOC concentrations were highest in laterally formed soils, including bedrock Histosols and E podzols, and DOC concentrations declined across the hillslope. Pardo et al. (2022) identified similar trends in DOC and acidity and found that bedrock-controlled areas acted as hotspots for elevated acidic DOC concentrations. Given that DOC within our study area has been shown to be effective at chelating Al (Fakhraei and Driscoll, 2015), a structural element in plagioclase, it likely plays an important role in facilitating the formation of a plagioclase weathering gradient.

Our results agree with the conceptual model proposed by Bailey et al. (2019a) based on streamwater chemistry measurements at HBEF, which proposes that mineral weathering is promoted by organic acids in shallow soils in the upper parts of the watershed. These organic acids are hypothesized to be partially neutralized by the products of weathering in bedrock Histosols and E podzols. Afterwards, they are hypothesized to precipitate with metals as organometallic complexes in Bhs podzols or be exported from upland soils into riparian and fluvial areas (Bailey et al., 2019a; Bourgault et al., 2017; Bourgault et al., 2015). Our work showing a plagioclase weathering gradient from E podzols to Bhs podzols to Typical podzols, therefore, supports the idea that shallow bedrock Histosols and E podzols act in concert as a "weathering engine" in the watershed. Groundwater that reaches E podzols is enriched with organic acids, has low mineral contact time, and undergoes frequent cycles of saturation and recession, in contrast to deeper soils, where groundwater rarely rises above the interface of the lower B horizon/ upper C horizon (Bailey et al., 2019a, 2014; Benton et al., 2022; Possinger et al., 2020). Overall, stream solute measurements indicate that long water residence times and increased soil thickness are the main factors controlling the export of dissolved weathering products (Johnson et al., 2000; Jutebring Sterte et al., 2021; Likens et al., 1998). Benettin et al. (2015) found that they needed to simulate subsurface mixing to depths of at least 3 m in Watershed 3 of HBEF in order to predict Si and Na concentrations using a catchment-scale solute transport model. Still, water younger than 30 days represented the overall driver of streamflow concentration dynamics. When comparing elemental losses among pedons, we find that weathering intensity is highest in laterally developed E podzols and Bhs podzols, where groundwater is highly responsive to precipitation and water-soil contact time is short, and which likely represent a significant fraction of young water (Figs. 2 and 3; Table 1; Benettin et al., 2015; Gannon et al., 2014).

The difference in τ between the most depleted (E podzol) and least depleted (Typical podzol) profiles is comparable to depletion differences between the oldest and youngest soils in glacial chronosequences in Europe and the western USA (Table 1; Fig. 3; Bain et al., 1993; Taylor and Blum, 1995). The highest Na and Ca losses estimated in this study exceed losses estimated for soils developed from postglacial parent material under a precipitation gradient in New Zealand (Dixon et al., 2016), with the upper end of precipitation more than triple that of HBEF (~4700 mm vs. 1400 mm). This suggests that climate (e.g., mean annual precipitation) is a poor predictor of chemical weathering intensity for the soils within our study. A key variable is the transition from shallow bedrock to deep soils. The impermeable nature of the soil-bedrock interface can facilitate much higher water fluxes in convergent zones of the upper part of the hillslope than in lower soils where bedrock is as much as 6 m deep. Because of this, the laterally developed soils in our study affected by shallow flowpaths likely receive higher water fluxes than predicted by precipitation or water availability alone.

The chemical weathering gradient we observed occurs in similaraged, closely spaced (40–200 m) soils affected by similar temperature and precipitation. This implies that water residence time and solution chemistry can be important factors in chemical weathering at the catchment scale. Our work, therefore, provides field-based support for findings from reactive transport modeling by Maher (2011). The organization of chemical weathering intensity in our system shows that pedogenesis is occurring laterally in the upper parts of the hillslope, emphasizing the need to account for patterns of soil development in topographically complex areas within models that include soil, hydrology, or weathering parameters.

5. Conclusions

Our work demonstrates that the progression of plagioclase weathering in temperate podzols is strongly connected to lateral spatial patterns in soil morphology that are reflective of local hydrology, solution chemistry, and topography. Hillslope trends in depletion of Na, Ca, and Al and mineralogical data reveal a gradient in plagioclase weathering that occurs along a catena. The influence of lateral flow on the weathering of plagioclase, the dominant Ca source in these soils, has significant implications for the biogeochemistry of Ca, an ecologically significant element that experienced historic depletion from soils in the Northeastern USA. The weathering gradient we discovered contradicts the dominant paradigm of soil weathering as occurring as a top-down process, showing that lateral patterns in eluviation and illuviation are pedogenically significant. Our work reinforces a need to incorporate lateral soil processes in landscape and soil development models.

Declaration of Competing Interest

The authors declare that they have no known competing financial interests or personal relationships that could have appeared to influence the work reported in this paper.

Acknowledgments

HBEF is located on unceded Abenaki land. HBEF is maintained and operated by the Northern Research Station of the USDA Forest Service, located in Madison, WI, USA. We thank Kinsey Ashe, Stephanie Duston, Joshua Benton, Nathaniel Rasnake, Pratt Olson, Elizabeth Beall, and Dan Needham for their assistance with field sampling and laboratory analysis. Olivia Fraser supplied soil maps and GIS data which helped us choose field sites. SEM imaging work was performed at the Microscopy Imaging Center at the University of Vermont (RRID# SCR_018821). EPMA was performed at the Department of Geosciences Electron Microprobe/SEM Facility at the University of Massachusetts. Keith Klepeis generously allowed the use of a whole-slide scanner. We appreciate the insightful comments of two anonymous reviewers and the Associate Editor that greatly improved the manuscript. We acknowledge Carleton Bern and Julia Perdrial for discussions that informed ideas in this manuscript. Scott Merrill and Nico Perdrial provided helpful comments on an early draft. Funding support for this study was provided by the National Science Foundation through the Geobiology and Low-Temperature Geochemistry program (EAR-1643415/1643327). Additional support was provided by a Sigma Xi Grant in Aid of Research and the Long-Term Ecological Research program (DEB-1637685).

Appendix A

Variation in C horizon and index element concentration

The number of C horizon samples collected within this study (17) enabled us to test the assumption that C horizon material is mineral-ogically homogenous with depth and remove outliers from the reference pool if significant deviation was observed. Although in some cases multiple samples were collected from the same pit, intra-pit elemental variation was comparable with inter-pit elemental variation and thus was not expected to add significant bias to the reference value. One deep C horizon was determined to have a titanium concentration that was

over 1.5 times the interquartile range (differing more than 2.7 standard deviations than the other samples) and was excluded from the reference pool. Two deep C horizon samples were enriched in silica over 1.5 times the interquartile range after calculating $\tau_{\rm Si}$ and were excluded from the reference pool. After removing these samples, elemental averages were determined from 14 remaining deep C horizon samples (representing samples obtained from the base of 5 soil pits and 3 deep well cores) and used as reference values for calculating τ .

Before estimating elemental depletion, variation in reference elements and C horizon composition was inspected. After evaluating Ti, Zr, and Nd as potential index elements, Ti and Zr were chosen for comparison because they were highest in concentration and thus less influenced by analytical error. Bern et al. (2011) used $R_{Ti/(Ti+Zr)}$ as a fingerprint to identify and quantify colloidal redistribution of material and reveal bias in the mass balance approach. In our samples, $R_{Ti/(Ti+Zr)}$ of C horizon samples varied randomly as expected for well-mixed sediments. When compared to the average $R_{Ti/(Ti+Zr)}$ of C horizon samples, two of the six E podzols were found to have the highest and lowest R_{Ti} $_{(Ti+Zr)}$ of all digested samples, located within 50 m of each other on the west side of the watershed (Table A1). Horizons in the pit with the highest $R_{\mathrm{Ti/(Ti+Zr)}}$ value contained Ti concentrations that were 25 % greater than other E podzols, Zr concentrations that were 28 % lower than other E podzols, and Na concentrations that were 46 % greater than other E podzols. Horizons in the other four E podzols had $R_{Ti/(Ti+Zr)}$ values that were consistent with the average R_{Ti/(Ti+Zr)} of C horizon samples. Bhs and Typical podzols showed similar patterns with depth. For the majority of Bhs and Typical pits, an increase in $R_{Ti/(Ti+Zr)}$ was observed in upper Bhs horizons, reflecting an increase in Ti relative to Zr, while fluctuations in $R_{Ti/(Ti+Zr)}$ were observed in the lower B horizons, reflecting increases and decreases in Zr relative to Ti (Table A1). In contrast, Zr concentrations remained relatively stable in upper horizons but exhibited jagged variability relative to Ti in lower Bhs, Bs, and BC horizons in 5 Bhs and Typical podzols. Since potentially nonweathering-derived variations in both index elements were detected, and Ti concentrations were more abundant and thus generally more consistent with depth in the lower B horizons, Ti was selected for use as an index element for estimating Na depletion.

Lithologic influences on index element concentration

Enrichment of Ti in Bhs horizons relative to overlying E horizons, though minor, was an unexpected finding, as Ti tends to concentrate within horizons experiencing the most weathering, which we would anticipate to be the E horizons in this system. The accumulation of amorphous organometallic complexes in the Bhs horizon would be expected to dilute Ti concentrations relative to E horizons. Increased Ti in Bhs horizons might be reflective of colloidal transport, a phenomenon that has been observed in the case of Ti within much older soils (Bern et al., 2015). Through SEM analysis, three Ti-bearing phases were identified: rutile, titanite, and ilmenite. On average, identifiable phases were present as 50-240 µm grains. Upon further examination of soil clods and the major till lithology, a minor proportion of biotite and chlorite possessed a sagenitic texture, defined by well-oriented, acicular inclusions of titanite and rutile (Shau et al., 1991; Fig. A3). These inclusions measured 1–10 μm \times 10–50 μm and could have precipitated during retrograde metamorphism of Kinsman granodiorite, the principal source lithology of the parent material. It is possible that during soil formation, fragments of colloidal titanite and rutile were released by dissolution of biotite and chlorite and physically transported from E horizons into Bhs horizons along with amorphous organometallic complexes. The needle-like acicular crystal habit could be more susceptible to physical breakdown than the non-sagenitic rounded grains otherwise encountered and thus more easily transported. The high organic matter content of Bhs horizons (up to 30 %) might be expected to increase the sensitivity of Ti concentrations to translocations, as there is less mineral content per mass unit soil. Regardless of the origin, any translocated Ti

would artificially inflate depletion estimates for Bhs horizons and depress depletion estimates for overlying or upslope E horizons, with the assumption that translocation processes are uniformly distributed and operate similarly to the movement of amorphous organometallic complexes in lateral and vertical settings. If this is the case, the significant differences we observed between lateral E and Bhs horizons would represent conservative estimates of actual differences in depletion. Using the same logic, Ti translocation may be responsible for the absence of a significant difference in depletion between vertical E and Bhs horizons. In contrast, variation in Zr content relative to Ti content would have significantly influenced depletion estimates for Bhs and Typical podzols on a per-solum basis if Zr had been selected as an index element. Spikes in Zr content may derive from minor sorting of glacial deposits during or shortly after deposition, as heavier minerals often settle out first. If Zr and Ti exhibited similar enrichment patterns in certain horizons, sorting would likely have a greater effect on Zr concentrations due to Zr being an order of magnitude lower in concentration than Ti, and due to the presence of Ti within minerals with a wider range of densities than Zr. Despite variation in both index elements, the age of these soils would be expected to limit the extent of colloidal redistribution. Increased Ti in Bhs horizons only led to a calculation of more intense depletion in Bhs horizons relative to E horizons in four of the nine pits with both horizons. This increase is close in proportion to the estimated error, and these horizons are generally thin, so the magnitude of this effect is expected to be small (Table A1).

The E podzol with unusually elevated Ti, elevated Ca, and the highest $R_{\mathrm{Ti/(Ti+Zr)}}$ values may reflect variation in the parent material. Though elevated, the concentrations of Ti and Ca within this pit are proportional to values observed in the other E podzols. Rock fragments containing sagenitic biotite and chlorite were observed in a nearby Bhs podzol, but not within the E podzol pit. No titanite was observed within the observable fine fraction of soil, and plagioclase constituted the dominant Na-bearing mineral, representing the highest proportion of Na observed. The low ratio of plagioclase to quartz observed for this soil and correspondingly high estimate of quartz-based plagioclase loss, like other E podzols, supports our Ti-based estimate of Na loss. Due to the thickness of the E horizon in E podzol soils and the magnitude of estimated losses, this pit still shows greater net depletion than Typical podzols for both Na and plagioclase on a per-depth basis.

Because storage of Na in secondary phases and exchange sites is low, and it is commonly used as a proxy for plagioclase, it was selected for the following additional calculations. The percentage of Na in each phase was multiplied by the mineral area of each phase to estimate the Na content of the mineral-only fraction. This was then divided by the sum of Na for all phases to estimate the percent contribution of each phase to the total. The Na contribution from each phase in mg kg $^{-1}$ was estimated by multiplying the Na contribution from each mineral by its abundance in mass percent. This was summed and total Na of each slide was compared to total Na obtained from elemental digestion.

Total Ca estimated from EPMA and Ca from total elemental digestion differed by a median amount of 21 % (Fig. A4). For all but two slides, EPMA-estimated Ca was lower than elemental digestion Ca. The greatest deviation between EPMA and digestion Ca was observed in an E podzol exhibiting high Ti and Ca content, followed by Bhs horizons with high concentrations of amorphous organometallic complexes. The smallest deviation was observed in E, Bs, and C horizons. Total Na estimated from EPMA and Na from total elemental digestion differed more, with a median difference of 49 %, and EPMA-estimated Na was lower for all thin sections (Fig. A4). As described in the paper, when Ca and Na were estimated from plagioclase content using the stoichiometry determined by SEM-EDS, total Ca and Na estimated by EPMA were closer to digestion Ca and Na than they were from pixel-based elemental estimates, with median differences of 12 % and 10 %, respectively.

Detailed procedures for quantifying mineralogy with SEM and EPMA

Edge artifacts, non-clod minerals embedded in epoxy, and clasts greater than 2 mm in size were removed from EPMA scans using FIJI before analysis (Schindelin et al., 2012). Beam intensity did not vary appreciably throughout the slide scan, due to the use of a newer microprobe instrument, so the procedure for averaging and correcting elemental counts described in Bailey et al. (2019b) was not necessary. Each set of scans was imported into Multispec (Biehl and Landgrebe, 2002) and converted to an 11-channel or a 5-channel image depending on whether the scan was a hypermap or a non-hypermap. To identify minerals, a clustering approach was performed in Multispec following the instructions of Lydon (2005). Cluster classification was performed on the whole image area, using a threshold of 25, and employed the ISODATA algorithm. Clusters were initiated within the eigenvector volume using a convergence of 98 %, a minimum cluster size of 11, and a starting number of 60 clusters. If 60 clusters were not enough to separate certain low-area minerals (for example, apatite and sphene), the process was re-run with a larger number of clusters, with 120 being the maximum.

To relate WDS-acquired elemental counts collected on a per-pixel basis with weight percent elemental content of mineral species, 3 high resolution small maps were collected at a 5 μm by 5 μm resolution. Small maps, chosen to represent a broad diversity of minerals, were selected from large maps of two soil thin sections, as well as from a large map thin section constructed from a local Rangeley schist bedrock core. Bedrock was included to enable access to larger grains and unaltered mineral surfaces. These focused maps allowed for targeting individual mineral grains of interest for spot WDS analysis, which revealed the stoichiometry and elemental content of each mineral. Pixel-based elemental counts from whole slide maps for each mineral of interest were then plotted against point elemental content and used to establish standard curves relating pixel elemental concentration to mineral elemental concentration for each of the five main (non-hypermap) elements of interest.

Our scripts for determining mineral identity through EPMA enabled us to detect void phases (sum of oxides < 9 %), non-crystalline materials such as amorphous organometallic complexes, and partition edge pixels into mineral and void fractions. It is important to note that estimated void content is overestimated for minerals composed of a significant proportion of elements that were not scanned with WDS (e.g., microcline, muscovite, apatite, due to these phases containing significant amounts of K and P), although this is not expected to have significantly altered the results of our analysis. Although the five elements selected for quantitative analysis represent the most common elements within these soils (excluding K, which was mapped with EDS), this approach excludes certain crystalline non-silicate minerals such as non-Ca-bearing phosphates (monazite) and non-Fe- and non-Al-bearing oxides (birnessite, rutile), although the abundance of these phases is trace (<1%) according to EPMA and SEM estimates. For phases containing less than 85 % oxides, the percent mineral content and percent void were estimated and converted to area units (number of pixels) before summing.

Peak deconvolution of EDS spectra was calibrated with an Astimex MINM25-53 standard puck with 53 embedded minerals, enabling semiquantitative estimation of elemental abundance and determination of mineral stoichiometry. In general, the elemental content estimated from pixel counts using standard curves was well correlated to SEM-EDS point analyses. Based on SEM groundtruthing, the identities of some clusters were manually changed to correct for the influence of high concentrations of amorphous organometallic complexes and amorphous oxides coating mineral grain edges, which inflated the iron and aluminum content of mineral pixels. Mineral identification was most accurate for abundant, large mineral grains that were composed of the elements analyzed by WDS (Ca, Al, Si, Fe, Na), such as plagioclase. Small proportions of less-common minerals with variable composition, such as garnet, pyroxene, and hornblende, were often classified within more

abundant phases such as chlorite, epidote, and actinolite, an effect that was reduced by expanding the number of clusters and ground-truthing mineral identity with SEM, but not eliminated entirely. The presence of amorphous organometallic complexes complicated efforts to measure muscovite and biotite, due to the compositional similarity between biotite mineral edges and muscovite mineral edges and amorphous organometallic complexes. For the most part, iterative SEM investigation resolved initial ambiguity within the EPMA cluster analyses. Identification of mineral phases with EPMA was most complete in solum horizons with less than 10 g kg⁻¹ organic matter predominated by mineral grains $>\!30~\mu m$ in diameter, achieving an identification success of over 90 % in 21/26 slides. Identification was less successful in C horizons, with 74-79 % (area %) mineral content identified despite a high density of crystalline minerals (up to 81 % of the total slide area). Identification success was also reduced in Bhs horizons, with these clods only containing 9-14 % crystalline mineral content within the total slide area. Low porosity and the difficulty of identifying mixed pixels containing the edges of closely packed adjoining phases lowered the success of mineral identification in C horizons. The composition of unidentified pixels, being mostly edge, is therefore probably close to the identified mineralogy.

References

- Anderson, R.S., Rajaram, H., Anderson, S.P., 2018. Climate driven coevolution of weathering profiles and hillslope topography generates dramatic differences in critical zone architecture. Hydrological Processes 33, 4–19. https://doi.org/ 10.1002/hyp.13307.
- April, R., Hluchy, M., Newton, R., 1986. The Nature of Vermiculite in Adirondack Soils and Till. Clays Clay Miner. - CLAYS CLAY Min. 34, 549–556. https://doi.org/ 10.1346/CCMN.1986.0340508.
- Bailey, S.W., Brousseau, P.A., McGuire, K.J., Ross, D.S., 2014. Influence of landscape position and transient water table on soil development and carbon distribution in a steep, headwater catchment. Geoderma 226–227, 279–289. https://doi.org/ 10.1016/j.geoderma.2014.02.017.
- Bailey A.S., Hornbeck J.W., Campbell J.L., Eagar C., 2003. Hydrometeorological database for Hubbard Brook Experimental Forest: 1955-2000. Gen Tech Rep NE-305 Newtown Sq. PA US Dep. Agric. For. Serv. Northeast. Res. Stn. 36 P 305. https://doi. org/10.2737/NE-GTR-305.
- Bailey S.W., Buso D.C., Likens G.E., 2003. Implications of Sodium Mass Balance for Interpreting the Calcium Cycle of a Forested Ecosystem. Ecology 84, 471–484. https://doi.org/10.1890/0012-9658(2003)084[0471:IOSMBF]2.0.CO;2.
- Bailey, S.W., McGuire, K.J., Ross, D.S., Green, M.B., Fraser, O.L., 2019a. Mineral Weathering and Podzolization Control Acid Neutralization and Streamwater Chemistry Gradients in Upland Glaciated Catchments. Northeastern United States. Front. Earth Sci. 7 https://doi.org/10.3389/feart.2019.00063.
- Bailey, S.W., Ross, D.S., Perdrial, N., Jercinovic, M., Webber, J., Bourgault, R., 2019b. Determination of Primary Mineral Content and Calcium Sources in Forest Soils using Electron Probe Microanalysis Mapping and Cluster Analysis. Soil Science Society of America Journal 83, 1830–1841. https://doi.org/10.2136/sssaj2019.07.0231.
- Bain, D.C., Mellor, A., Robertson-Rintoul, M.S.E., Buckland, S.T., 1993. Variations in weathering processes and rates with time in a chronosequence of soils from Glen Feshie, Scotland. Geoderma 57, 275–293. https://doi.org/10.1016/0016-7061(93) 90010-1.
- Barker, F., 1961. Phase relations in cordierite-garnet-bearing kinsman quartz monzonite and the enclosing schist, lovewell mountain quadrangle, New Hampshire. American Mineralogist 46, 1166–1176.
- Beaudette, D.E., Roudier, P., O'Geen, A.T., 2013. Algorithms for quantitative pedology: A toolkit for soil scientists. Computational Geosciences 52, 258–268. https://doi.org/ 10.1016/j.cageo.2012.10.020.
- Bel, J., Legout, A., Saint-André, L., Hall, S.J., Löfgren, S., Laclau, J.-P., van der Heijden, G., 2020. Conventional analysis methods underestimate the plant-available pools of calcium, magnesium and potassium in forest soils. Scientific Reports 10, 15703. https://doi.org/10.1038/s41598-020-722741-w.
- Benettin, P., Bailey, S.W., Campbell, J.L., Green, M.B., Rinaldo, A., Likens, G.E., McGuire, K.J., Botter, G., 2015. Linking water age and solute dynamics in streamflow at the Hubbard Brook Experimental Forest, NH, USA. Water Resources Research 51, 9256–9272. https://doi.org/10.1002/2015WR017552.
- Benton, J.R., McGuire, K.J., Schreiber, M.E., 2022. Subsurface permeability contrasts control shallow groundwater flow dynamics in the critical zone of a glaciated, headwater catchment. Hydrological Processes 36, e14672.
- Bern, C.R., Chadwick, O.A., Hartshorn, A.S., Khomo, L.M., Chorover, J., 2011. A mass-balance model to separate and quantify colloidal and solute redistributions in soil. Chemical Geology 282, 113–119. https://doi.org/10.1016/j.chemgeo.2011.01.014.
- Bern, C.R., Thompson, A., Chadwick, O.A., 2015. Quantification of colloidal and aqueous element transfer in soils: The dual-phase mass balance model. Geochimica et Cosmochimica Acta 151, 1–18. https://doi.org/10.1016/j.gca.2014.12.008.

- Biehl, L., Landgrebe, D., 2002. MultiSpec: a tool for multispectral-hyperspectral image data analysis. Computational Geosciences 28, 1153–1159. https://doi.org/10.1016/ S0098-3004(02)00033-X.
- Bourgault, R.R., Ross, D.S., Bailey, S.W., 2015. Chemical and Morphological Distinctions between Vertical and Lateral Podzolization at Hubbard Brook. Soil Science Society of America Journal 79, 428–439. https://doi.org/10.2136/sssaj2014.05.0190.
- Bourgault, R.R., Ross, D.S., Bailey, S.W., Bullen, T.D., McGuire, K.J., Gannon, J.P., 2017. Redistribution of soil metals and organic carbon via lateral flowpaths at the catchment scale in a glaciated upland setting. Geoderma 307, 238–252. https://doi. org/10.1016/j.geoderma.2017.05.039.
- Bower J.A., Pennino A.M., Bailey S.W., McGuire K.J., Duston S.A., 2023a. Hubbard Brook Experimental Forest: Watershed 3 Lateral Weathering Pedon Descriptions. https://doi.org/10.6073/PASTA/ED5326149D2FEA068D6C8D4D550718EC.
- Bower J.A., Pennino A.M., McGuire K.J., 2023b. Hubbard Brook Experimental Forest: Watershed 3 Lateral Weathering Soil Chemistry. https://doi.org/10.6073/PASTA/7348AB7D97A765B612687BA547A7AA47.
- Bower J.A., 2023. Tau value generator for soils sampled for the Lateral Weathering project at Hubbard Brook. https://doi.org/10.5281/zenodo.7510625.
- Brantley, S., White, A., 2009. Approaches to Modeling Weathered Regolith. Rev. Mineral. Geochem. - REV Miner. GEOCHEM 70, 435–484. https://doi.org/10.2138/ rmg.2009.70.10.
- Brimhall, G.H., Christopher, J.L., Ford, C., Bratt, J., Taylor, G., Warin, O., 1991.
 Quantitative geochemical approach to pedogenesis: importance of parent material reduction, volumetric expansion, and eolian influx in lateritization. Geoderma, Weathering of Soils 51 (1–4), 51–91.
- Brimhall, G.H., Dietrich, W.E., 1987. Constitutive mass balance relations between chemical composition, volume, density, porosity, and strain in metasomatic hydrochemical systems: Results on weathering and pedogenesis. Geochimica et Cosmochimica Acta 51, 567–587. https://doi.org/10.1016/0016-7037(87)90070-6.
- Burton, W.C., Walsh, G.J., Armstrong, T.R., 2000. Bedrock geologic map of the Hubbard
 Brook Experimental Forest, Grafton County, New Hampshire [electronic resource].
 U.S. Department of the Interior, U.S. Geological Survey.
- Chadwick, O.A., Gavenda, R.T., Kelly, E.F., Ziegler, K., Olson, C.G., Elliott, W.C., Hendricks, D.M., 2003. The impact of climate on the biogeochemical functioning of volcanic soils. Chem. Geol. Controls on Chemical Weathering 202, 195–223. https:// doi.org/10.1016/j.chemseo.2002.09.001.
- Chauvel, A., Lucas, Y., Boulet, R., 1987. On the genesis of the soil mantle of the region of Manaus, Central Amazonia, Brazil. Experientia 43, 234–241. https://doi.org/ 10.1007/BF01945546.
- Deer, W.A., Howie, R.A., Zussman, J. (Eds.), 2013. An Introduction to the Rock-Forming Minerals. Mineralogical Society of Great Britain and Ireland.
- Delvigne, J.E., 1998. Atlas of Micromorphology of Mineral Alteration and Weathering. Mineralogical Association of Canada.
- Dixon, J.L., Chadwick, O.A., Vitousek, P.M., 2016. Climate-driven thresholds for chemical weathering in postglacial soils of New Zealand. Journal of Geophysical Research - Earth Surface 121, 1619–1634. https://doi.org/10.1002/2016JF003864.
- Do Nascimento, N.R., Fritsch, E., Bueno, G.T., Bardy, M., Grimaldi, C., Melfi, A.J., 2008. Podzolization as a deferralitization process: dynamics and chemistry of ground and surface waters in an Acrisol – Podzol sequence of the upper Amazon Basin. European Journal of Soil Science 59, 911–924. https://doi.org/10.1111/j.1365-2389.2008.01049.x.
- Fakhraei, H., Driscoll, C.T., 2015. Proton and Aluminum Binding Properties of Organic Acids in Surface Waters of the Northeastern U.S. Environmental Science & Technology 49, 2939–2947. https://doi.org/10.1021/es504024u.
- Federer, C.A., Hornbeck, J.W., Tritton, L.M., Martin, C.W., Pierce, R.S., Smith, C.T., 1989. Long-term depletion of calcium and other nutrients in eastern US forests. Environmental Management 13, 593–601. https://doi.org/10.1007/BF01874965.
- Federer, C.A., Turcotte, D.E., Smith, C.T., 1993. The organic fraction-bulk density relationship and the expression of nutrient content in forest soils. Canadian Journal of Forest Research 23 (6), 1026–1032.
- Ferrier, K.L., Kirchner, J.W., Riebe, C.S., Finkel, R.C., 2010. Mineral-specific chemical weathering rates over millennial timescales: Measurements at Rio Icacos, Puerto Rico. Chemical Geology 277, 101–114. https://doi.org/10.1016/j. chemgeo.2010.07.013.
- Fraser, O.L., Bailey, S.W., Ducey, M.J., McGuire, K.J., 2020. Predictive modeling of bedrock outcrops and associated shallow soil in upland glaciated landscapes. Geoderma 376, 114495.
- Freer, J., McDonnell, J.J., Beven, K.J., Peters, N.E., Burns, D.A., Hooper, R.P., Aulenbach, B., Kendall, C., 2002. The role of bedrock topography on subsurface storm flow. Water Resources Research 38 (12), 5-1–5-16.
- Fritsch, E., Balan, E., Régina Do Nascimento, N., Allard, T., Bardy, M., Bueno, G., Derenne, S., Melfi, A.J., Calas, G., 2011. Deciphering the weathering processes using environmental mineralogy and geochemistry: Towards an integrated model of laterite and podzol genesis in the Upper Amazon Basin. Comptes Rendus Geosci. 343 (2,3) 188-198
- Gannon, J.P., Bailey, S.W., McGuire, K.J., 2014. Organizing groundwater regimes and response thresholds by soils: A framework for understanding runoff generation in a headwater catchment. Water Resources Research 50, 8403–8419. https://doi.org/ 10.1002/2014WR015498.
- Gannon, J.P., Bailey, S.W., McGuire, K.J., Shanley, J.B., 2015. Flushing of distal hillslopes as an alternative source of stream dissolved organic carbon in a headwater catchment. Water Resources Research 51, 8114–8128. https://doi.org/10.1002/ 2015WP016927
- Gannon, J.P., McGuire, K.J., Bailey, S.W., Bourgault, R.R., Ross, D.S., 2017. Lateral water flux in the unsaturated zone: A mechanism for the formation of spatial soil

- heterogeneity in a headwater catchment. Hydrological Processes 31, 3568–3579. https://doi.org/10.1002/hyp.11279.
- Gillin, C.P., Bailey, S.W., McGuire, K.J., Gannon, J.P., 2015a. Mapping of Hydropedologic Spatial Patterns in a Steep Headwater Catchment. Soil Science Society of America Journal 79, 440–453. https://doi.org/10.2136/ sssai2014.05.0189
- Gillin, C.P., Bailey, S.W., McGuire, K.J., Prisleyt, S.P., 2015b. Evaluation of Lidar-derived DEMs through Terrain Analysis and Field Comparison. Photogrammetric Engineering & Remote Sensing 81, 387–396. https://doi.org/10.14358/ PERS.81.5.387.
- Harman, C.J., Cosans, C.L., 2019. A low-dimensional model of bedrock weathering and lateral flow coevolution in hillslopes: 2. Controls on weathering and permeability profiles, drainage hydraulics, and solute export pathways. Hydrological Processes 33, 1168–1190. https://doi.org/10.1002/hyp.13385.
- Jankowski, M., 2014. The evidence of lateral podzolization in sandy soils of Northern Poland. CATENA, Landscapes and Soils through Time 112, 139–147. https://doi. org/10.1016/j.catena.2013.03.013.
- Jersak, J., Amundson, R., Brimhall, G., 1995. A mass balance analysis of podzolization: Examples from the northeastern United States. Geoderma 66 (1-2), 15–42.
- Johnson, C.E., Driscoll, C.T., Siccama, T.G., Likens, G.E., 2000. Element Fluxes and Landscape Position in a Northern Hardwood Forest Watershed Ecosystem. Ecosystems 3, 159–184. https://doi.org/10.1007/s100210000017.
- Jongmans, A.G., van Breemen, N., Lundström, U., van Hees, P.A.W., Finlay, R.D., Srinivasan, M., Unestam, T., Giesler, R., Melkerud, P.-A., Olsson, M., 1997. Rockeating fungi. Nature 389 (6652), 682–683.
- Jutebring Sterte, E., Lidman, F., Balbarini, N., Lindborg, E., Sjöberg, Y., Selroos, J.-O., Laudon, H., 2021. Hydrological control of water quality – Modelling base cation weathering and dynamics across heterogeneous boreal catchments. The Science of the Total Environment 799, 149101. https://doi.org/10.1016/j. scitotenv.2021.149101.
- Leyval, C., Berthelin, J., 1991. Weathering of a Mica by Roots and Rhizospheric Microorganisms of Pine. Soil Science Society of America Journal 55, 1009–1016. https://doi.org/10.2136/sssai1991.03615995005500040020x.
- Likens, G.E., Driscoll, C.T., Buso, D.C., Siccama, T.G., Johnson, C.E., Lovett, G.M., Fahey, T.J., Reiners, W.A., Ryan, D.F., Martin, C.W., Bailey, S.W., 1998. The biogeochemistry of calcium at Hubbard Brook. Biogeochemistry 41, 89–173. https://doi.org/10.1023/A:1005984620681.
- Lin, H.S., Kogelmann, W., Walker, C., Bruns, M.A., 2006. Soil moisture patterns in a forested catchment: A hydropedological perspective. Geoderma, Hydropedology: Bridging Disciplines, Scales and Data 131, 345–368. https://doi.org/10.1016/j. geoderma.2005.03.013.
- LoRusso, N.A., Bailey, S.W., Zeng, T., Montesdeoca, M., Driscoll, C.T., 2021. Dissolved Organic Matter Dynamics in Reference and Calcium Silicate-Treated Watersheds at Hubbard Brook Experimental Forest, NH, USA. J. Geophys. Res. Biogeosciences 126, e2021JG006352. https://doi.org/10.1029/2021JG006352.
- Lydon, J., 2005. The measurement of the modal mineralogy of rocks from SEM imagery: the use of Multispec© and ImageJ freeware. https://doi.org/10.4095/220706.
- Maher, K., 2010. The dependence of chemical weathering rates on fluid residence time. Earth and Planetary Science Letters 294, 101–110. https://doi.org/10.1016/j.epsl.2010.03.010.
- Maher, K., 2011. The role of fluid residence time and topographic scales in determining chemical fluxes from landscapes. Earth and Planetary Science Letters 312, 48–58. https://doi.org/10.1016/j.epsl.2011.09.040.
- McGuire, K.J., McDonnell, J.J., Weiler, M., Kendall, C., McGlynn, B.L., Welker, J.M., Seibert, J., 2005. The role of topography on catchment-scale water residence time. Water Resources Research 41. https://doi.org/10.1029/2004WR003657.
- Nezat, C.A., Blum, J.D., Klaue, A., Johnson, C.E., Siccama, T.G., 2004. Influence of landscape position and vegetation on long-term weathering rates at the Hubbard Brook Experimental Forest, New Hampshire, USA. Geochim. Cosmochim. Acta 68, 3065–3078. https://doi.org/10.1016/j.gca.2004.01.021.
- Nezat, C.A., Blum, J.D., Yanai, R.D., Hamburg, S.P., 2007. A sequential extraction to determine the distribution of apatite in granitoid soil mineral pools with application to weathering at the Hubbard Brook Experimental Forest, NH. USA. Appl. Geochem. 22, 2406–2421. https://doi.org/10.1016/j.apgeochem.2007.06.012.
- Norton, K.P., Molnar, P., Schlunegger, F., 2014. The role of climate-driven chemical weathering on soil production. Geomorphology 204, 510–517. https://doi.org/10.1016/j.geomorph.2013.08.030.
- Pardo L.H., Green M.B., Bailey S.W., McGuire K.J., McDowell W.H., 2022. Identifying Controls on Nitrate Sources and Flowpaths in a Forested Catchment Using a Hydropedological Framework. J. Geophys. Res. Biogeosciences 127, e2020JG006140. https://doi.org/10.1029/2020JG006140.
- Park, S.J., Burt, T.P., 2002. Identification and characterization of pedogeomorphological processes on a hillslope. Soil Science Society of America Journal 66 (6), 1897–1910.
- Possinger, A.R., Bailey, S.W., Inagaki, T.M., Kögel-Knabner, I., Dynes, J.J., Arthur, Z.A., Lehmann, J., 2020. Organo-mineral interactions and soil carbon mineralizability with variable saturation cycle frequency. Geoderma 375, 114483. https://doi.org/ 10.1016/j.geoderma.2020.114483.
- R Core Team, 2022. R: A Language and Environment for Statistical Computing.Rasmussen, C., Brantley, S., Richter, D.deB., Blum, A., Dixon, J., White, A.F., 2011.Strong climate and tectonic control on plagioclase weathering in granitic terrain.Earth and Planetary Science Letters 301 (3-4), 521–530.
- Remondi, F., Botter, M., Burlando, P., Fatichi, S., 2019. Variability of transit time distributions with climate and topography: A modelling approach. Journal of Hydrology 569, 37–50. https://doi.org/10.1016/j.jhydrol.2018.11.011.
- Richter, D.D., Comer, P.J., King, K.S., Sawin, H.S., Wright, D.S., 1988. Effects of Low Ionic Strength Solutions on pH of Acid Forested Soils. Soil Science Society of America

- Journal 52, 261–264. https://doi.org/10.2136/sssaj1988.03615995005200010046x.
- Salve, R., Rempe, D.M., Dietrich, W.E., 2012. Rain, rock moisture dynamics, and the rapid response of perched groundwater in weathered, fractured argillite underlying a steep hillslope. Water Resources Research 48. https://doi.org/10.1029/ 2012WR012583
- Schindelin, J., Arganda-Carreras, I., Frise, E., Kaynig, V., Longair, M., Pietzsch, T., Preibisch, S., Rueden, C., Saalfeld, S., Schmid, B., Tinevez, J.-Y., White, D.J., Hartenstein, V., Eliceiri, K., Tomancak, P., Cardona, A., 2012. Fiji: an open-source platform for biological-image analysis. Nature Methods 9, 676–682. https://doi.org/ 10.1038/mmeth.2019.
- Schoeneberger P.J., Wysocki D.A., Benham E.C., National Soil Survey Center (U.S.) (Eds.), 2012. Field book for describing and sampling soils, Version 3.0. ed. National Soil Survey Center, Natural Resources Conservation Service, U.S. Department of Agriculture, Lincoln, Nebraska.
- Shau, Y.-H., Yang, H.-Y., Peacor, D.R., 1991. On oriented titanite and rutile inclusions in sagenitic biotite. American Mineralogist 76, 1205–1217.
- Slessarev, E.W., Feng, X., Bingham, N.L., Chadwick, O.A., 2019. Landscape Age as a Major Control on the Geography of Soil Weathering. Glob. Biogeochem. Cycles 33, 1513–1531. https://doi.org/10.1029/2019GB006266.
- Soil Survey Staff, 2022. Keys to Soil Taxonomy, 13th ed. Department of Agriculture, Natural Resources Conservation Service, Washington, D.C.
- Sommer, M., Halm, D., Weller, U., Zarei, M., Stahr, K., 2000. Lateral Podzolization in a Granite Landscape. Soil Science Society of America Journal 64 (6), 2069.
- Sommer, M., Halm, D., Geisinger, C., Andruschkewitsch, I., Zarei, M., Stahr, K., 2001. Lateral podzolization in a sandstone catchment. Geoderma 103, 231–247. https://doi.org/10.1016/S0016-7061(01)00018-0.
- Stoops, G., 2021. Guidelines for Analysis and Description of Soil and Regolith Thin Sections. John Wiley & Sons.
- Stoops, G., Altemueller, H.J., Bisdom, E.B.A., Delvigne, J., Dobrovolsky, V.V., Fitzpatrick, E.A., Paneque, G., Sleeman, J., 1979. Guidelines for the description of mineral alterations in soil micromorphology. Pedologie 29 (1), 121–135.
- Taboada, T., Cortizas, A.M., García, C., García-Rodeja, E., 2006. Particle-size fractionation of titanium and zirconium during weathering and pedogenesis of

- granitic rocks in NW Spain. Geoderma 131, 218–236. https://doi.org/10.1016/j.geoderma.2005.03.025.
- Taylor, A., Blum, J.D., 1995. Relation between soil age and silicate weathering rates determined from the chemical evolution of a glacial chronosequence. Geology 23, 979–982. https://doi.org/10.1130/0091-7613(1995)023<0979:RBSAAS>2.3.CO;2.
- van der Meij, W.M., Temme, A.J.A.M., Lin, H.S., Gerke, H.H., Sommer, M., 2018. On the role of hydrologic processes in soil and landscape evolution modeling: concepts, complications and partial solutions. Earth Science Reviews 185, 1088–1106. https:// doi.org/10.1016/j.earscirev.2018.09.001.
- VandenBygaart, A.J., Gregorich, E.G., Angers, D.A., McConkey, B.G., 2007. Assessment of the lateral and vertical variability of soil organic carbon. Canadian Journal of Soil Science 87, 433–444. https://doi.org/10.4141/CJSS06025.
- Villars, T.R., Bailey, S.W., Ross, D.S., 2015. Four Soil Orders on a Vermont Mountaintop—One-Third of the World's Soil Orders in a 2500-Square-Meter Research Plot. Soil Horiz. 56 https://doi.org/10.2136/sh15-06-0013.
- Wallman, P., Svensson, M.G.E., Sverdrup, H., Belyazid, S., 2005. ForSAFE—an integrated process-oriented forest model for long-term sustainability assessments. For. Ecol. Manag. Decision Support in Multi Purpose Forestry 207, 19–36. https://doi.org/10.1016/j.foreco.2004.10.016
- Weyman, D.R., 1973. Measurements of the downslope flow of water in a soil. Journal of Hydrology 20, 267–288. https://doi.org/10.1016/0022-1694(73)90065-6.
- White, A.F., Bullen, T.D., Schulz, M.S., Blum, A.E., Huntington, T.G., Peters, N.E., 2001. Differential rates of feldspar weathering in granitic regoliths. Differential Rates of Feldspar Weathering in Granitic Regoliths. 65 (6), 847–869.
- Wickham, H., 2007. Reshaping Data with the reshape Package. Journal of Statistical Software 21, 1–20. https://doi.org/10.18637/jss.v021.i12.
- Wickham, H., Averick, M., Bryan, J., Chang, W., McGowan, L.D., François, R., Grolemund, G., Hayes, A., Henry, L., Hester, J., Kuhn, M., Pedersen, T.L., Miller, E., Bache, S.M., Müller, K., Ooms, J., Robinson, D., Seidel, D.P., Spinu, V., Takahashi, K., Vaughan, D., Wilke, C., Woo, K., Yutani, H., 2019. Welcome to the Tidyverse. J. Open Source Softw. 4, 1686. https://doi.org/10.21105/joss.01686.
- Yoo, K., Mudd, S.M., 2008. Discrepancy between mineral residence time and soil age: Implications for the interpretation of chemical weathering rates. Geology 36, 35–38. https://doi.org/10.1130/G24285A.1.